

# Data-Driven Joint Inversions for PDE Models

Kui Ren\*      Lu Zhang<sup>†</sup>

## Abstract

The task of simultaneously reconstructing multiple physical coefficients in partial differential equations from observed data is ubiquitous in applications. In this work, we propose an integrated data-driven and model-based iterative reconstruction framework for such joint inversion problems where additional data on the unknown coefficients are supplemented for better reconstructions. Our method couples the supplementary data with the PDE model to make the data-driven modeling process consistent with the model-based reconstruction procedure. We characterize the impact of learning uncertainty on the joint inversion results for two typical model inverse problems. Numerical evidences are provided to demonstrate the feasibility of using data-driven models to improve joint inversion of physical models.

**Key words.** Computational inverse problems, joint inversion, data-driven models, machine learning, iterative reconstruction, sensitivity analysis, PDE-constrained optimization

**AMS subject classifications 2010.** 35R30, 49M41, 65M32, 65N21, 68Q32, 68T07, 78A46

## 1 Introduction

Let  $X$  and  $Y$  be two spaces of functions, and  $\mathcal{A}_h : X \times X \mapsto Y$  an operator between them, depending on the parameter  $h \in H$ . We consider the following abstract inverse problem of reconstructing  $f \in X$  and  $g \in X$  from measured data encoded in  $u_h \in Y$ :

$$\mathcal{A}_h(f, g) = u_h. \quad (1)$$

We will make the forward operator  $\mathcal{A}$  more explicit when discussing concrete inverse problems. For the moment, we assume that the operators  $\mathcal{A}_h(f, \cdot)$  and  $\mathcal{A}_h(\cdot, g)$  are both uniquely invertible at given  $f$  and  $g$  in  $X$ .

This types of inverse problem appears in many applications where  $f$  and  $g$  are physical quantities that we are interested in imaging from measured data  $u_h$ . For instances, in diffuse

---

\*Department of Applied Physics and Applied Mathematics, Columbia University, New York, NY 10027; [kr2002@columbia.edu](mailto:kr2002@columbia.edu)

<sup>†</sup>Department of Applied Physics and Applied Mathematics, Columbia University, New York, NY 10027; [lz2784@columbia.edu](mailto:lz2784@columbia.edu)

optical tomography [3],  $f$  and  $g$  could be respectively the optical absorption and scattering coefficients of the underlying medium to be probed. In photoacoustic imaging [35, 13, 44, 29, 5, 39],  $f$  and  $g$  could be respectively the ultrasound speed and the optical absorption coefficient of the medium. In geophysical applications such as seismic imaging [12, 19, 24],  $f$  and  $g$  could be respectively the velocity field and the density field of the Earth. We refer interested readers to [8, 11, 33, 43, 23, 42] and references therein for more examples of such multiple-coefficient inverse problems. In Section 3, we will present two concrete examples of such inverse problems.

In many applications, we face the issue that when  $f$  and  $g$  are treated as independent variables, the data available in  $\{u_h\}_{h \in \mathcal{H}}$  are not sufficient to reconstruct  $f$  and  $g$  simultaneously. This is the situation in diffuse optical tomography where boundary current data are not enough to uniquely determine both the absorption and the scattering coefficients of the underlying medium [3]. Even when the available data are sufficient to uniquely determine the two coefficients, the inversion process could be unstable. One therefore has to introduce additional information in order to improve such joint inversions.

There are roughly two lines of ideas in the literature for joint inversion. The first type of methods introduces additional measurement data to enrich the information content of data  $\{u_h\}$ . The additional measurement could come from either the same physics in the original problem [39] or a different but related physical process that is coupled to the original problem [1, 17, 30] (often called model fusion). The second type of methods uses *a priori* information we have on the unknown  $f$  and  $g$  to improve the reconstruction. This includes, for instance, structural methods where one assumes that  $f$  and  $g$  share the same structural features that one can impose in the reconstruction process through regularization; see [12, 18] and references therein.

In some physical applications,  $f$  and  $g$  are physical coefficients that are related to each other either because they describe physical properties that are connected together or because their values change in a similar way in response to an environmental change. For instance, in diffuse optical tomography, the optical absorption and scattering coefficients of the tissues to be probed change in a correlated way when tumorous cells are developed. In such a case, one can potentially utilize the relation between the coefficients to improve the computational reconstruction of them. In the rest of this work, we consider the situation where we have a large amount of past data on  $f$  and  $g$  that allow us to learn some simplified relation, denoted by  $\mathcal{N}_\theta$ , parameterized by  $\theta$ , between features of  $f$  and  $g$ . We then use this learned relation to help the simultaneous reconstruction of  $f$  and  $g$ . Let  $\mathcal{F}(f)$  represent the part of information on  $f$  that would like to link with the same information on  $g$ , then the process can be written mathematically as

$$\mathcal{F}(g) = \mathcal{N}_\theta(\mathcal{F}(f)). \quad (2)$$

The operator  $\mathcal{F}$  is decided by given *a priori* knowledge on the physics of the problem. Examples of  $\mathcal{F}$  for practical applications include, for instance, the gradient operator for situations where only the gradient of the  $f$  and  $g$  are expected to be related [12], and the truncated Fourier transform for applications where only some (lower) Fourier modes between  $f$  and  $g$  are expected to be related. In the simplest case where  $\mathcal{F}$  is invertible,  $\mathcal{F}^{-1} \circ \mathcal{N}_\theta \circ \mathcal{F}$

gives the relation between the original coefficients  $f$  and  $g$ .

## 2 Computational framework

The joint inversion problem we introduced can be summarized as follows. Given a set of,  $N$ , historical coefficient pairs

$$\{f_k, g_k\}_{k=1}^N, \quad (3)$$

and a set of new measured data

$$\{u_h\}_{h \in H} \quad (4)$$

corresponding to the mathematical model (1), we are interested in reconstructing the functions  $f$  and  $g$  corresponding to the measurements (4).

The inversion process with data (3) and (4) is a two-step procedure. In the first step, we learn from data (3) a relation  $\mathcal{N}_\theta$  between  $\mathcal{F}(f)$  and  $\mathcal{F}(g)$  as given in (2), while in the second step, we use this relation and data (4) to reconstruct the coefficients  $f$  and  $g$ . Our idea is philosophically similar to the idea of learning a regularization functional from historical data, such as those in [21], but is fundamentally different in terms of the details of the implementation, including how the learning process is done and how the learned model is utilized in the joint inversion stage.

### 2.1 Model-consistent data-driven learning

The first stage of the inversion is a modeling process where we use existing historical data (3) to learn the relation  $\mathcal{N}_\theta$ . This process is done independent of the reconstruction process. This is similar to the works where one learns a regularization functional based on the available data [21]. However, given that the relation  $\mathcal{N}_\theta$  we learned will be used in model-based inversion with data (4) in the next step, it is advantageous to make the modeling process consistent with the inversion procedure. Therefore, we perform the modeling step taking the physical model (1) as a constraint in addition to existing data (3). More precisely, we first pass the data (3) through the mathematical model (1) to obtain the new training dataset

$$\{f_k, \{u_{h,k}\}_{h \in H}\}_{k=1}^N, \quad (5)$$

where the data point  $u_{h,k}$  is obtained by evaluating the forward model (1) with coefficient pair  $(f_k, g_k)$  and parameter  $h$ , that is,  $u_{h,k} = \mathcal{A}_h(f_k, g_k)$ . We then use this new dataset as the additional training dataset to impose consistency between the learned model  $\mathcal{N}_\theta$  and the forward model (1). The learning process is realized by solving the following minimization problem:

$$\begin{aligned} \hat{\theta} &= \arg \min_{\theta \in \Theta} \mathcal{L}(\theta), \\ \mathcal{L}(\theta) &:= \frac{1}{2N|H|} \sum_{h \in H} \sum_{k=1}^N \|\mathcal{A}_h(f_k, \tilde{\mathcal{N}}_\theta(f_k)) - u_{h,k}\|_Y^2 + \frac{1}{2N} \sum_{k=1}^N \|\mathcal{F}(g_k) - \mathcal{N}_\theta(\mathcal{F}(f_k))\|_{\tilde{X}}^2. \end{aligned} \quad (6)$$

where  $\tilde{\mathcal{N}}_\theta := \mathcal{F}^{-1} \circ \mathcal{N}_\theta \circ \mathcal{F}$  is the relation between the coefficients  $f$  and  $g$  in the physical space  $X$ .

This computational optimization problem is by no means easy to solve as it is generally non-convex (since the relation  $\mathcal{N}_\theta$  is most likely nonlinear) and the dimension of the problem can be very high. It is critical to select efficient representations for both the functions  $f$  and  $g$ , and the relation between them, that is the operator  $\mathcal{N}_\theta$ . Our objective in this proof of concept study is not to develop such representations for a given problem, but rather to show that with reasonable parameterization of the objects involved, we can have a feasible learning procedure that can be useful for joint reconstructions in the next stage of the computational procedure.

We consider in the rest of this work parameterization of the functions  $f$  and  $g$  by their Fourier coefficients. More precisely, we take  $\mathcal{F}(f)$  to be the  $K$ -term truncated generalized Fourier series of  $f$  in the sense that

$$\mathcal{F}(f) = \sum_{k=1}^K \hat{f}_k \varphi_k(\mathbf{x}) \quad (7)$$

where  $\varphi_k(\mathbf{x})$  is the eigenfunctions of the Laplace operator with Neumann boundary condition, that is,

$$-\Delta \varphi_k = \lambda_k \varphi_k(\mathbf{x}), \quad \text{in } \Omega, \quad \mathbf{n} \cdot \nabla \varphi_k(\mathbf{x}) = 0, \quad \text{on } \partial\Omega. \quad (8)$$

When  $\Omega$  is smooth,  $\{\varphi_k\}_{k \geq 1}$  forms an orthonormal basis in  $\mathcal{L}^2(\Omega)$ ; see for instance [28]. We can thus identify any function  $f$  with its corresponding generalized Fourier coefficient vector  $\hat{\mathbf{f}} = (\hat{f}_1, \dots, \hat{f}_K)$  and attempt to learn a nonlinear relation between the generalized Fourier coefficients of  $f$  and  $g$ :

$$\mathcal{N}_\theta : \begin{array}{ccc} \hat{\mathbf{f}} & \mapsto & \hat{\mathbf{g}} \\ \mathbb{R}^K & \mapsto & \mathbb{R}^K, \end{array}$$

where  $K$  is relatively small (as we are not attempting to learn precise relations but only reasonably good approximations to help the joint reconstructions in the next step of this data-driven joint inversion procedure), to be specified later in the numerical experiments. We consider two different parameterizations of the relation  $\mathcal{N}_\theta$ .

We implement two different representations of the map  $\mathcal{N}_\theta$ . The first representation of  $\mathcal{N}_\theta$  is through multi-dimensional polynomials. Let  $\boldsymbol{\alpha} = (\alpha_1, \dots, \alpha_K)$  be a multi-index,  $|\boldsymbol{\alpha}| := \sum_{i=1}^K \alpha_i$ , and  $P_{\boldsymbol{\alpha}}(\hat{\mathbf{f}})$  be the monomial of order  $\boldsymbol{\alpha}$  formed from  $\hat{\mathbf{f}}$ , that is,

$$P_{\boldsymbol{\alpha}}(\hat{\mathbf{f}}) := \prod_{k=1}^K \hat{f}_k^{\alpha_k}.$$

Then the specific polynomial model we take can be written in the form:

$$\hat{\mathbf{g}} = \mathcal{N}_\theta(\hat{\mathbf{f}}) := \left( \sum_{|\boldsymbol{\alpha}| \leq n} \theta_{1,\boldsymbol{\alpha}} P_{\boldsymbol{\alpha}}(\hat{\mathbf{f}}), \dots, \sum_{|\boldsymbol{\alpha}| \leq n} \theta_{j,\boldsymbol{\alpha}} P_{\boldsymbol{\alpha}}(\hat{\mathbf{f}}), \dots, \sum_{|\boldsymbol{\alpha}| \leq n} \theta_{K,\boldsymbol{\alpha}} P_{\boldsymbol{\alpha}}(\hat{\mathbf{f}}) \right) \quad (9)$$

where  $n$  is the order of the polynomial, and  $\{\theta_{j,\boldsymbol{\alpha}}\}_{j=1}^K$  is the set of coefficients of the polynomials. In the numerical simulations, we are interested in limiting the size of the parameter

space of the problem. To limit the size of parameter space, we will impose sparsity constraints on the coefficient tensor, as the precise relation between the coefficients is not what we are interested in representing. The details will be provided in Appendix A.1.

The second representation of  $N_\theta$  that we implemented, as a feasibility study and also as a benchmark to the first approach, is a fully connected neural network. We adopt a standard autoencoder network architecture. The learning network contains three major substructures: an encoder network  $E_\theta$ , a decoder network  $D_\theta$ , and an additional predictor network  $P_\theta$ . The encoder-decoder substructure is trained to regenerate the input data, while the predictor reads the latent variable to predict the velocity field. In terms of the input-output data, the network is trained such that  $\hat{\mathbf{f}} = D_\theta(E_\theta(\hat{\mathbf{f}}))$  and  $\hat{\mathbf{g}} = P_\theta(E_\theta(\hat{\mathbf{f}}))$ . Once the training is performed, the learned model is  $\mathcal{N}_{\hat{\theta}} := P_{\hat{\theta}} \circ E_{\hat{\theta}}$ . We provided more details on the implementation of the network structure as well as the training process in Appendix A.2.

## 2.2 Joint reconstruction

We can now perform joint inversion of  $f$  and  $g$  from given noisy data  $\{u_h^\delta\}$ ,  $\delta$  indicates the level of random noise in the data, with the learned relation  $\mathcal{N}_{\hat{\theta}}$ . We perform the reconstruction with the classical model-based iterative inversion framework where we pursue the reconstruction by minimizing the mismatch between measured data and the model predictions. Instead of using the learned relation between  $f$  and  $g$  as a hard constraint in the inversion process, we use it as a guidance of the reconstruction. We start with the initial solution where we force the relation  $\mathcal{N}_{\hat{\theta}}$  exactly in the reconstruction. That is, we reconstruct  $(\hat{f}, g := \mathcal{N}_{\hat{\theta}}(\hat{f}))$  with  $\hat{f}$  given by

$$\hat{f}_0 = \arg \min_{f \in X} \Phi_0(f) := \frac{1}{2|\mathcal{H}|} \sum_{h=1}^{|\mathcal{H}|} \|\mathcal{A}_h(f, \mathcal{N}_{\hat{\theta}}(f)) - u_h^\delta\|_Y^2 + \frac{\gamma}{2} \|f\|_X^2. \quad (10)$$

We then reconstruct a sequence of  $(\hat{f}_j, \hat{g}_j)$  by solving

$$(\hat{f}_j, \hat{g}_j) = \arg \min_{(f, g) \in X \times X} \Phi_j(f, g), \quad (11)$$

where

$$\Phi_j(f, g) := \frac{1}{2|\mathcal{H}|} \sum_{h=1}^{|\mathcal{H}|} \|\mathcal{A}_h(f, g) - u_h^\delta\|_Y^2 + \frac{\alpha_j}{2} \|g - \mathcal{N}_{\hat{\theta}}(f)\|_X^2 + \frac{\gamma}{2} \|(f, g)\|_X^2. \quad (12)$$

We summarize the process in Algorithm 1.

There are two major reasons for us to not strictly enforce the relation  $\mathcal{N}_{\hat{\theta}}$ , that is, not directly taking the solution to (10) as the reconstruction result, in the inversion process. First, since the data-driven modeling process is not necessarily accurate, we want to allow the reconstruction process to search around  $(\hat{f}_0, \mathcal{N}_{\hat{\theta}}(\hat{f}_0))$  for coefficients that can potentially match the data better. Second, if Algorithm 1 yields a solution that is dramatically different than  $(\hat{f}_0, \mathcal{N}_{\hat{\theta}}(\hat{f}_0))$ , it is an indication that the admissible coefficient pairs for the new data do

---

**Algorithm 1** Joint Inversion with Learned Data Model

---

- 1: Evaluate  $\widehat{f}_0$  according to (10) and  $\widehat{g}_0 := \mathcal{N}_{\widehat{\theta}}(\widehat{f}_0)$
  - 2: Set  $\alpha_0$ ;
  - 3: **for**  $j = 1$  to  $j = J$  **do**
  - 4:     Set  $\alpha_j = \alpha_{j-1}/2$ ;
  - 5:     Evaluate  $(\widehat{f}_j, \widehat{g}_j)$  according to (11) using  $(\widehat{f}_{j-1}, \widehat{g}_{j-1})$  as the initial guess
  - 6: **end for**
- 

not live in the set  $(f, \mathcal{N}_{\theta}(f))$ . We therefore have to let the data to decide where what the solution is, not the prior knowledge we have from past training data.

To solve the minimization problems (10) and (11), we employed a classical BFGS quasi-Newton method that we implemented and benchmarked in [38].

### 3 Two model joint inversion problems

In this section, we introduce two examples of the abstract inverse problem (1). We will use the two examples for numerical simulations to demonstrate the performance of the data-driven joint inversion approach we proposed in the previous section.

#### 3.1 An inverse diffusion problem

In the first case, we consider a simplified inverse problem in quantitative photoacoustic imaging [5]. Let  $\Omega \subset \mathbb{R}^d$  ( $d \geq 1$ ) be a bounded domain representing an optical medium whose absorption and diffusion coefficients are respectively  $\sigma(\mathbf{x})$  and  $\gamma(\mathbf{x})$ . The transport of near infra-red photons inside the medium can be described by the following diffusion equation

$$\begin{aligned} -\nabla \cdot \gamma(\mathbf{x})\nabla u(\mathbf{x}) + \sigma(\mathbf{x})u(\mathbf{x}) &= 0, & \text{in } \Omega \\ \mathbf{n} \cdot \gamma\nabla u + \ell u(\mathbf{x}) &= S(\mathbf{x}), & \text{on } \partial\Omega \end{aligned} \tag{13}$$

where  $u(\mathbf{x})$  is the density of the photons at  $\mathbf{x}$  and  $S(\mathbf{x})$  is the illuminating source function sending photons into the medium. The vector  $\mathbf{n}(\mathbf{x})$  is the unit outer normal vector of  $\partial\Omega$  at  $\mathbf{x}$ , and the parameter  $\ell$  is known to be the inverse (re-scaled) extrapolation length.

The inverse problem is to reconstruct  $\sigma$  and  $\gamma$  from measured internal data of the form

$$H(\mathbf{x}) = \sigma(\mathbf{x})u(\mathbf{x}), \quad \mathbf{x} \in \bar{\Omega}. \tag{14}$$

This inverse problem is a simplified model of quantitative photoacoustic tomography, a hybrid acoustic-optical imaging modality where ultrasound measurements are used to get internal data (14); see for instance [5] and references therein for more recent overviews in this direction. The same diffusion model, but with additional boundary current data is also very useful in practical applications such as diffuse optical tomography [3]. It is well-known that there is an equivalence between  $\sigma$  and  $\gamma$  in the diffusion equation that prevents the unique

reconstruction of the pair  $(\sigma, \gamma)$  from a given datum  $H$  [5]. It has also been shown [5, 6] that  $\sigma$  and  $\gamma$  can be uniquely reconstructed with two well-selected datasets when  $\gamma$  is known on the boundary of the domain. If that is not the case, then uniqueness with two datasets can not hold [39]. In the rest of this work, we consider the case where additional data on the coefficients  $\sigma$  and  $\gamma$  are available to allow us to learn a relation between  $\sigma$  and  $\gamma$  that would help the online reconstruction of the coefficients.

### 3.2 An inverse wave propagation problem

The second example joint inversion problem we consider here is an inverse problem for the acoustic wave equation. Let  $\kappa$  and  $\rho$  be respectively the bulk modulus and the density of the underlying medium  $\Omega \subset \mathbb{R}^d$ , and  $p$  be the acoustic pressure due to a boundary source  $S(t, \mathbf{x})$ . Then  $p$  solves the following equation:

$$\begin{aligned} \frac{1}{\kappa} \frac{\partial^2 p}{\partial t^2} - \nabla \cdot \left( \frac{1}{\rho} \nabla p \right) &= 0, & \text{in } \mathbb{R}_+ \times \Omega \\ \mathbf{n} \cdot \frac{1}{\rho} \nabla p &= S(t, \mathbf{x}), & \text{on } \mathbb{R}_+ \times \partial\Omega \\ p(0, \mathbf{x}) = \frac{\partial p}{\partial t}(0, \mathbf{x}) &= 0, & \text{in } \Omega \end{aligned} \tag{15}$$

This wave propagation model, with slightly changes in boundary and initial conditions, serves as the forward model for inverse problems in seismic imaging [2, 10, 14, 15, 32, 37, 45, 46], medical ultrasound imaging [4, 9, 22, 27, 31, 34, 36, 47], among many other applications.

The inverse problem of interests [12, 19, 24] is to reconstruct the coefficients  $\kappa$  and  $\rho$  of the underlying medium from measured field  $u$  on the boundary of the medium:

$$H(t, \mathbf{x}) := p(t, \mathbf{x})|_{(0,T] \times \partial\Omega} \tag{16}$$

for a period of time  $T$  that is sufficiently long.

There is an extensive literature on the mathematical, computational and practical sides of this inverse problem; see the references cited above. In most case, the problem is simplified by assuming that  $\rho$  is constant so that the velocity field  $c$  of the wave, defined through  $\kappa = \rho c^2$ , is the effective coefficient to be reconstructed. Here we consider the case that historical data on the pair  $(\kappa, \rho)$  are available for us to learn a relation between  $\kappa$  and  $\rho$  to improve the online reconstruction of the pair of coefficients. This is similar to the past studies on the same problem with prior on the geometrical similarity of the coefficients [12].

## 4 Numerical experiments

We now present some numerical simulations to demonstrate the feasibility of proposed approach. Due to the proof-of-concept nature of this work, we will only work on synthetic data, meaning that the training data as well as the joint inversion data are constructed

through numerical simulations instead of real physical experiments. Our main point is to demonstrate that if there is indeed a physical law  $\mathcal{N}$  between the coefficients, the proposed data-driven joint reconstruction strategy can be a competitive alternative in solving joint inversion problems.

## 4.1 The inverse diffusion problem

We start with the inverse diffusion problem (13)–(14) introduced in Section 3.1. For simplicity of presentation, we set the extrapolation length  $\ell = 1$  as the particular value of the parameter has no impact on the results. We take the computational domain to be  $\Omega = (0, 1) \times (0, 1)$ , and discretize the problem with a  $P_1$  finite element method. The mesh is constructed such that the vertices are on the Cartesian grids defined by  $(x_i, y_j) = (i\Delta x, j\Delta y)$ ,  $i, j = 0, 1, \dots, M$  with  $\Delta x = \Delta y = 1/M$ .

**Numerical Experiment (I).** For the first numerical example, we consider the coefficients  $(\gamma, \sigma)$  of the forms, in the Fourier domain,

$$\gamma(\mathbf{x}) = \tilde{\gamma}_0 + \sum_{k_x, k_z=0}^K \gamma_{\mathbf{k}} \phi_{\mathbf{k}}(x, z), \quad \sigma(\mathbf{x}) = \tilde{\sigma}_0 + \sum_{k_x, k_z=0}^K \sigma_{\mathbf{k}} \phi_{\mathbf{k}}(x, z) \quad (17)$$

where  $\mathbf{k} = (k_x, k_z)$  and  $\phi_{\mathbf{k}}(x, z) = \cos(k_x \pi x) \cos(k_z \pi z)$  are the eigenfunctions in (8) for the domain  $\Omega = (0, 1)^2$ . We assume that the generalized Fourier coefficients are related by

$$\sigma_{\mathbf{k}} = \sum_{k'_x, k'_z=0}^K \mathbf{a}_{\mathbf{k}, \mathbf{k}'} \sin(\pi(2 + \gamma_{\mathbf{k}'})^{k_x + k_z}). \quad (18)$$

This relation is sufficiently smooth to be approximated with polynomials of relatively low orders.

**Learning dataset generation.** We generate a set of  $N = 10^4$  coupled diffusion-absorption fields  $\{\gamma_j, \sigma_j\}_{j=1}^N$  based on the relation (18). More precisely, we randomly choose the coefficients  $\{\gamma_{\mathbf{k}}\}_{\mathbf{k} \in \mathbb{N}_0 \times \mathbb{N}_0}$  from the uniform distribution  $\mathcal{U}[-0.5, 0.5]$ , and for each  $\mathbf{k}$  we pick  $\{\mathbf{a}_{\mathbf{k}, \mathbf{k}'}\}_{\mathbf{k}' \in \mathbb{N}_0 \times \mathbb{N}_0}$  from the uniform distribution  $\mathcal{U}[0, 0.1]$  to construct  $\sigma_{\mathbf{k}}$ . To impose the constraint on nonnegativity of the coefficients, we rescale the coefficients linearly to make them in the right range of values. In Figure 1 we show some typical samples of the  $(\gamma, \sigma)$  pair generated from (17)–(18).

**Learning and testing performance.** To learn the nonlinear relation  $\mathcal{N}$  between  $\gamma$  and  $\sigma$ , we perform a standard training-validation cycle on the neural network approximate nonlinear relation. Precisely, before the training process starts, we randomly split the synthetic dataset of  $N = 10^4$  data points into a training dataset and a testing dataset. Moreover, the training dataset takes 80% of the original dataset, and the test dataset takes the rest 20% of the data points. In Figure 2, we show three randomly selected absorption fields  $\sigma$  from the testing dataset which are generated by the diffusion fields  $\gamma$  based on (18), the corresponding neural

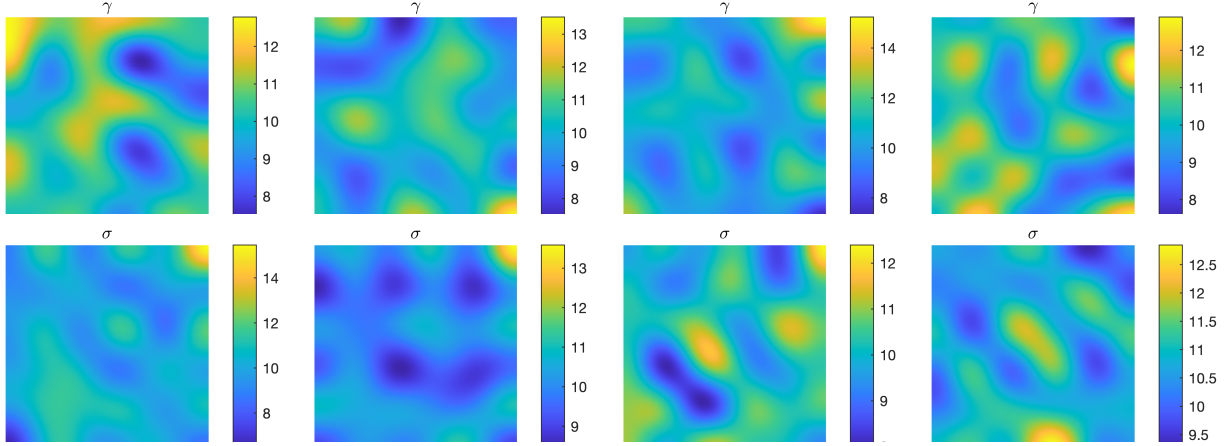


Figure 1: Four random samples of the  $\gamma$  (top) and  $\sigma$  (bottom) pair generated from (17)-(18) with  $K = 5$  for the learning stage of Numerical Experiment (I).

network predictions, and the errors in the prediction. We also present the training-validation loss curves in Figure 3. To save the presentation space, we only show the training-validation loss curves for the Fourier modes  $\sigma_{0,0}$ ,  $\sigma_{3,3}$ ,  $\sigma_{5,5}$ ,  $\sigma_{1,2}$ ,  $\sigma_{3,4}$ , and  $\sigma_{5,3}$  but we observe very similar curves for other Fourier modes. A quick takeaway from Figure 2 and Figure 3 is that the training process is quite successful as the testing errors are pretty reasonable, especially given that our training dataset is very small, only  $0.8 \times 10^4$  data points.

**Data-driven joint inversion.** With the learned relation between  $\gamma$  and  $\sigma$ , we perform joint reconstructions of  $(\gamma, \sigma)$  from internal data (14). The internal data are again synthetic; see Figure 4 for the datum  $H$  generated with the boundary source

$$S(\mathbf{x}) = e^{-\frac{(x-0.5)^2}{0.25}}, \quad \mathbf{x} = (x, y). \quad (19)$$

We implemented Algorithm 1 along with a BFGS reconstruction algorithm for (10) and (11) which we use the MATLAB inline function `fmincon` with the ‘bfgs’ option. In particular, the hyper-parameters  $(J, \alpha_0)$  in Algorithm 1 is set to be  $(J, \alpha_0) = (3, 0)$ , and the termination tolerances are set to be  $10^{-7}$  for the first-order optimality condition, and  $10^{-7}$  for the norm of the updating step size. In addition, we add the Gaussian noise with zeros mean and 5% standard derivation to test the stability of the proposed scheme.

Figure 5 presents the surface plots of the initial data for the step one of the reconstruction, i.e. solution to the optimization problem (10), and step two, i.e. solution to the optimization problem (11) with data collected from four different illumination sources supported on the four sides of the square  $\Omega = (0, 1)^2$ . To be precise, the first column shows the initial data for searching the diffusion field  $\gamma$  when solving (10). From the second to the fourth column, we plot the initial data for searching the diffusion coefficient  $\gamma$  (top) and the absorption field  $\sigma$  (bottom) when solving (11). Note that these data are obtained by solving (10) and then apply the learned nonlinear relation  $\mathcal{N}_{\hat{\theta}}$ ; see the first step in Algorithm 1. In particular, the second column presents the initial profiles generated from noise-free data, the third column shows the initial profiles reconstructed from the data with 5% additive Gaussian noise, and

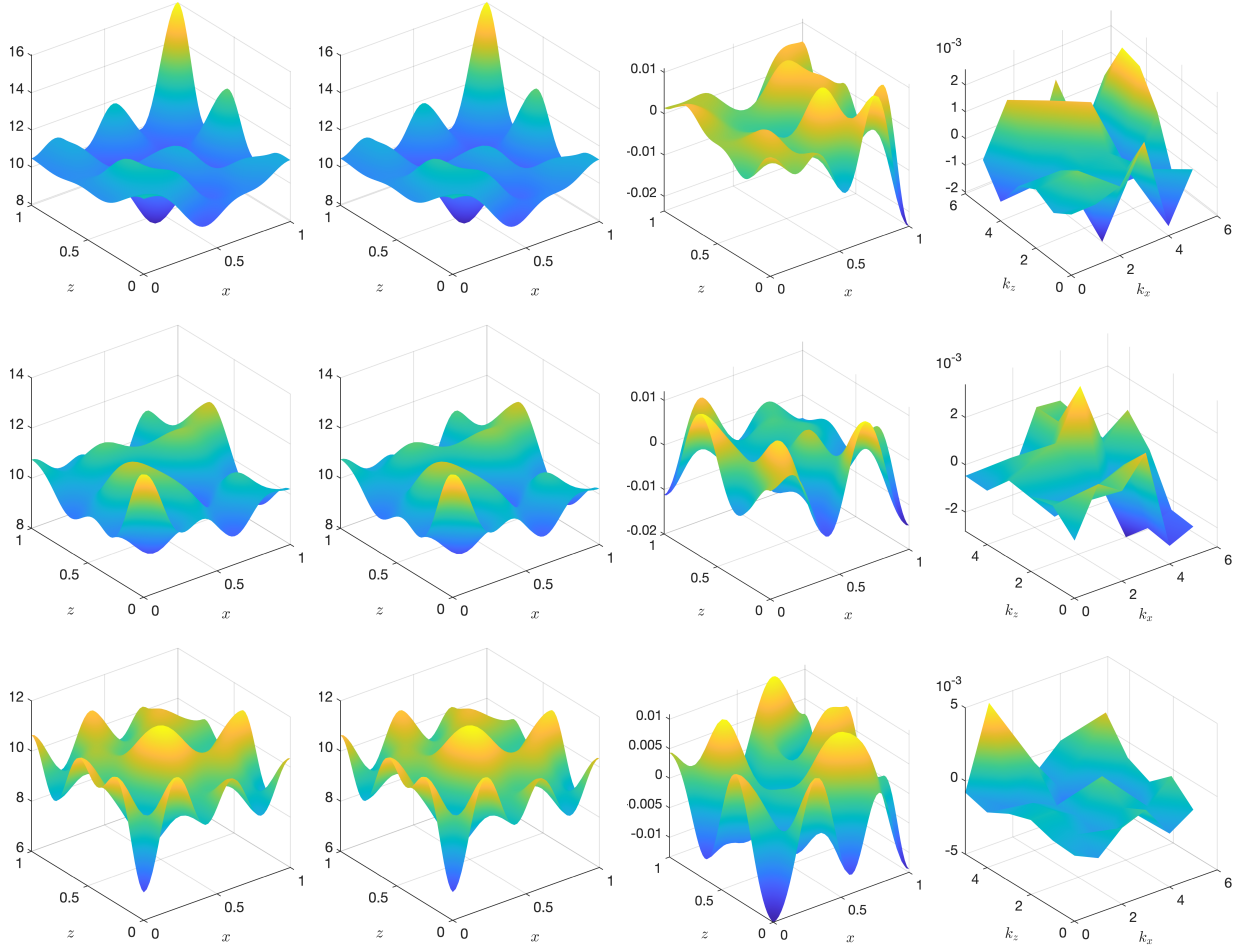


Figure 2: Three randomly selected absorption fields ( $\sigma$ ) from the testing dataset:  $6 \times 6$ -coefficient Fourier model in Numerical Experiment (I). From the left to the right are the exact absorption field (column 1), the predicted absorption field by the trained neural network (column 2), the error of the prediction in the physical space (column 3), and the error in the network prediction in the Fourier domain (column 4).

the fourth column displays the initial profiles assembled by the data with 5% multiplication Gaussian noise.

In Figure 6, we show the surface plots of the exact and the reconstructed  $\gamma$  and  $\sigma$  fields from the proposed data-driven joint inversion scheme. Specifically, we display the diffusion fields at the top panel, and the absorption fields are plotted at the bottom panel. From the left to the right are the surface plots of the true coefficients (first column); the reconstructed diffusion/absorption fields with noise-free internal data (second column), with the internal data containing 5% additive Gaussian noise (third column), and with the internal data including 5% multiplication Gaussian noise (fourth column). We observe that the accuracy of the reconstruction of the proposed joint inversion scheme is pretty well. Even with the noisy internal data, we can recover the main features of the diffusion coefficient  $\gamma$  and the absorption field  $\sigma$ .

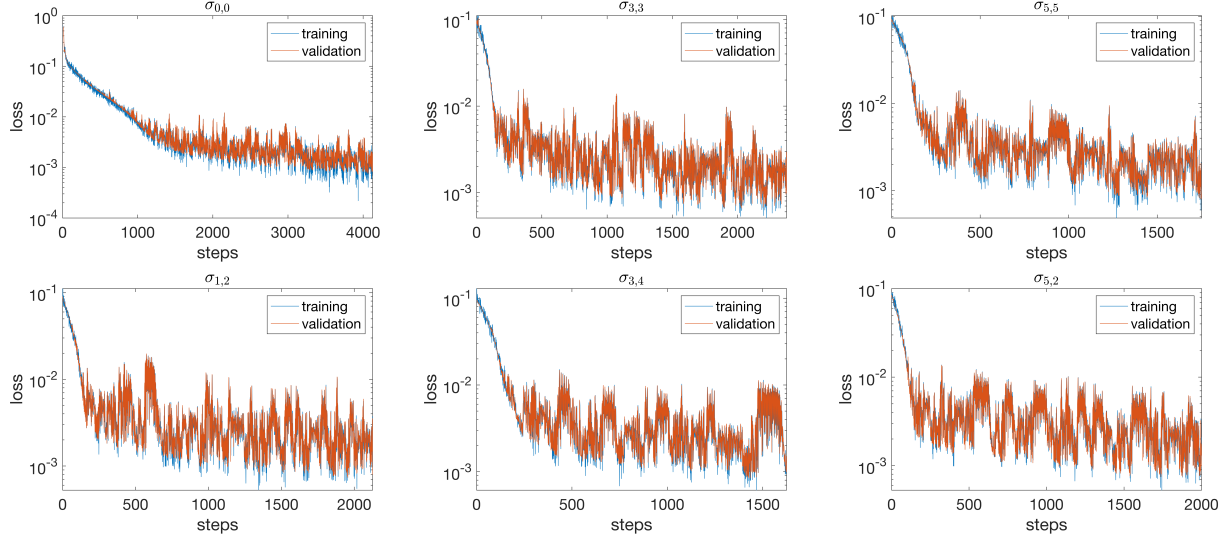


Figure 3: From the left to the right are the training and validation loss curves for the Fourier modes  $\sigma_{0,0}$ ,  $\sigma_{3,3}$ , and  $\sigma_{5,5}$  (top), and  $\sigma_{1,2}$ ,  $\sigma_{3,4}$ , and  $\sigma_{5,2}$  (bottom) of example one in Numerical Experiment (I). Very similar curves are observed for the training experiments of other Fourier modes.

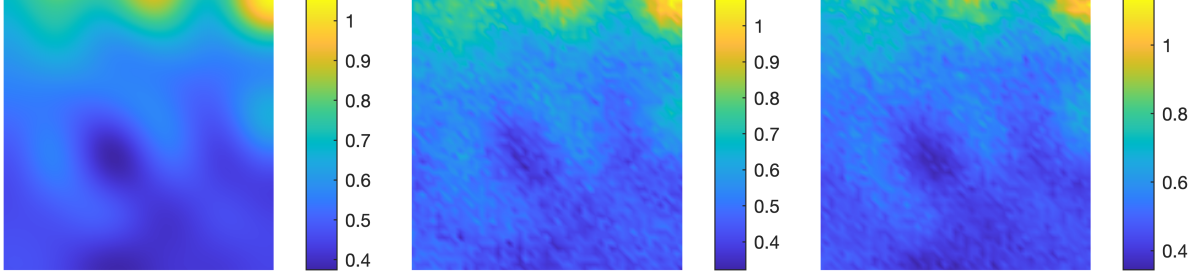


Figure 4: Internal datum  $H$  generated with illumination (19). From the left to the right are the noise-free recorded internal data, the recorded internal data with 5% additive Gaussian noise, and the recorded internal data with 5% multiplication Gaussian noise.

**Numerical Experiment (II).** In the second numerical example, we consider the diffusion coefficient  $\gamma$  and the absorption coefficient  $\sigma$  both as Gaussian functions. Precisely, they have the following relation

$$\gamma(\mathbf{x}) = b_1 + b_2 e^{-\frac{(x-b_4^1)^2 + (z-b_5^1)^2}{2b_3^2}}, \quad \sigma(\mathbf{x}) = c_1 + c_2 e^{-\frac{(x-c_4^2)^2 + (z-c_5^2)^2}{2c_3^2}}, \quad (20)$$

where

$$c_1 = \sum_{j=1}^5 a_{1j} \cos(10\pi b_j) + 8, \quad (21)$$

$$c_2 = 5 \sum_{j=1}^5 a_{2j} \cos(20\pi b_j) + 2.5, \quad c_3 = 0.1 \sum_{j=1}^5 a_{3j} \cos(30\pi b_j) + 0.2, \quad (22)$$

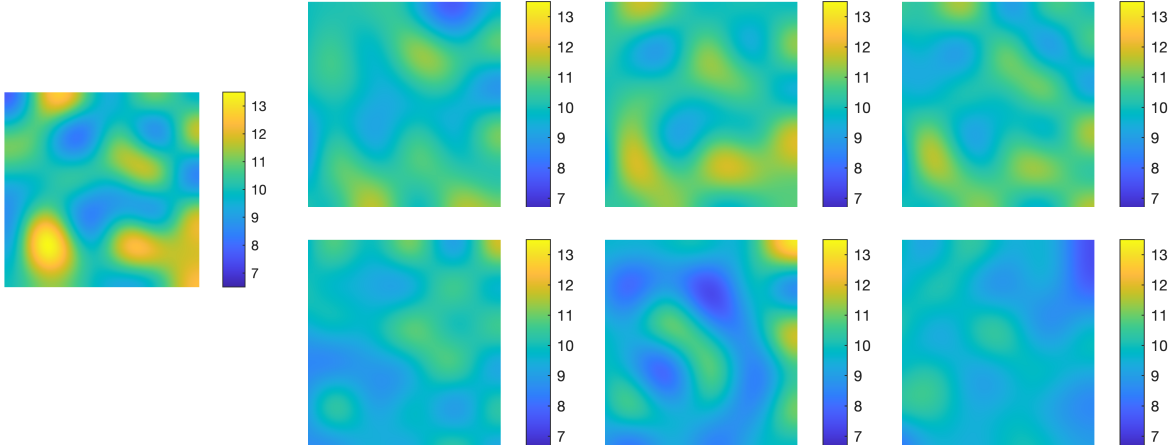


Figure 5: Reconstructions at each stage of the inversion process in Numerical Experiment (I). From left to right are: the initial reconstruction of  $\gamma$  as the solution to (10) (first column), the first step of reconstruction of  $(10^3\gamma, 50\sigma)$  by (11) with noise-free data (second column), with data containing 5% additive Gaussian noise (third column), and with data containing 5% of multiplicative Gaussian noise.

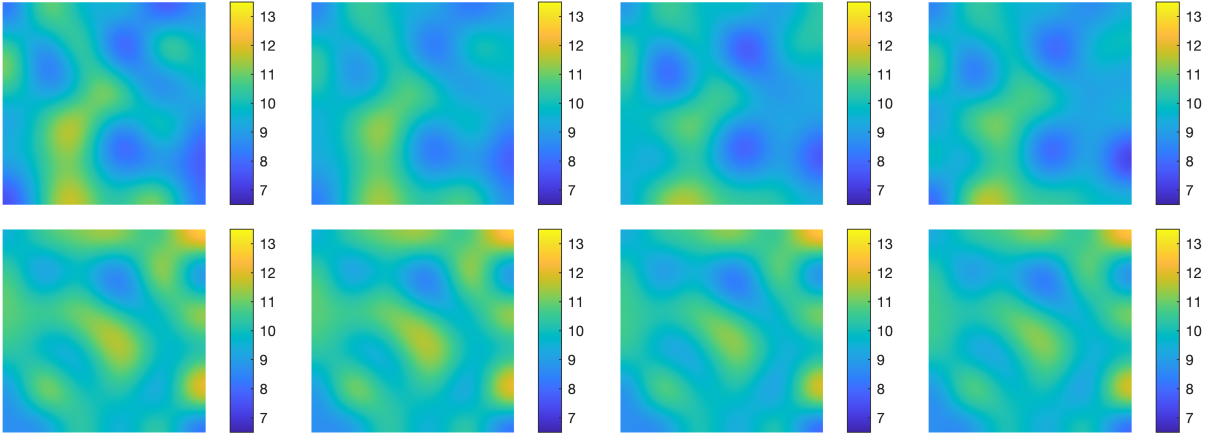


Figure 6: Joint inversion of  $(10^3\gamma, 50\sigma)$  in Numerical Experiment (I). Shown from left to right are: true coefficients, reconstruction from noise-free data, reconstruction from data with 5% additive Gaussian noise, and reconstruction from data with 5% multiplication Gaussian noise.

$$c_4 = \begin{cases} 0.5 \sum_{j=1}^5 a_{4j} \cos(40\pi b_j) + 0.75, & x \in [0, 0.5], \\ 0.5 \sum_{j=1}^5 a_{4j} \cos(40\pi b_j) + 0.25, & x \in (0.5, 1], \end{cases} \quad (23)$$

$$c_5 = \begin{cases} 0.5 \sum_{j=1}^5 a_{5j} \cos(50\pi b_j) + 0.75, & y \in [0, 0.5], \\ 0.5 \sum_{j=1}^5 a_{5j} \cos(50\pi b_j) + 0.25, & y \in (0.5, 1], \end{cases} \quad (24)$$

and  $a_{i,j} \in \mathcal{U}[0, 0.1]$  for  $i, j = 1, 2, \dots, 5$ . Note that in this case, even though the dimension of the feature space of both  $\gamma$  and  $\sigma$  is only 5, the nonlinear mapping  $\mathcal{N}$  between them is a piecewise function, which increases the potential difficulty of the training process. For the offline training, we generate a dataset of  $N = 4 \times 10^4$  for the pair of  $(\gamma, \sigma)$ , which is 3 times larger than that in Numerical Experiment (I), but in general is still small.

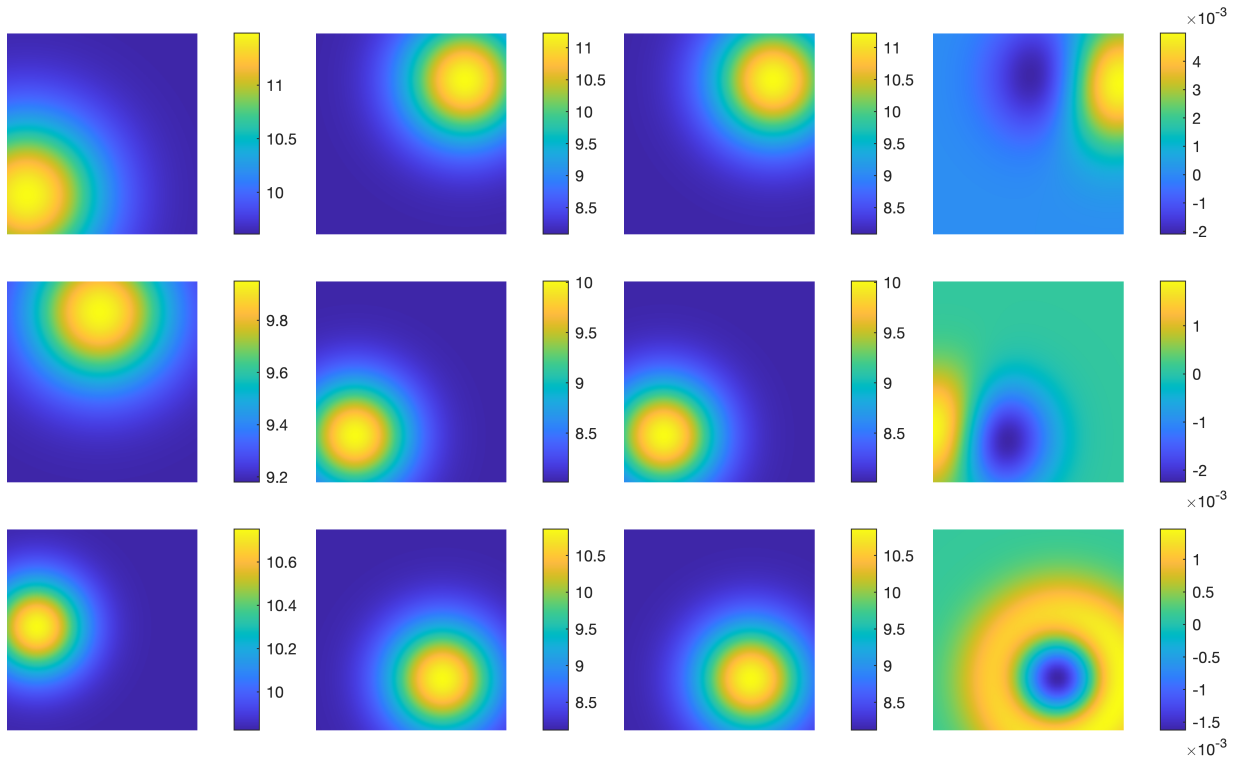


Figure 7: Three randomly selected diffusion fields  $\gamma$  from the testing dataset and the corresponding absorption fields  $\sigma$  for Numerical Experiment (II). From the left to the right are: the exact  $\gamma$ , the corresponding exact  $\sigma$ , the  $\sigma$  predicted by the trained neural network, and the error between the true and the network prediction.

We perform the same type of training as in Numerical Experiment (I) and will not repeat the details on training and validation. To demonstrate the success in learning, in Figure 7 we present the prediction of three randomly selected absorption fields  $\sigma$  from the testing dataset which are generated by the diffusion fields  $\gamma$  based on (20)-(24). From the left to the right, we show the true diffusion fields, the corresponding exact absorption fields, the corresponding neural network predictions of the absorption fields, and the errors in the prediction. We see that the training process is pretty successful regarding to the accuracy

of the prediction. Indeed, we also observe the training-validation loss curves for the training of the nonlinear relation between  $\{b_j\}$  and  $\{c_j\}$  very similar to those displayed in Figure 3.

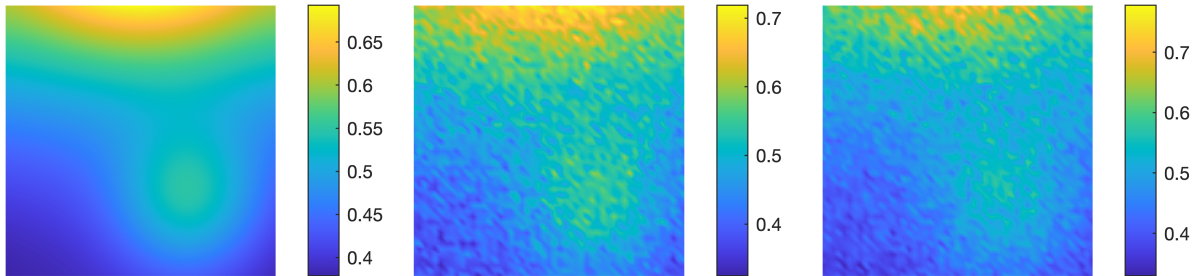


Figure 8: Internal data  $H$  generated with illuminating source (19) for Numerical Experiment (II). From the left to the right are respectively noise-free data, data with 5% additive Gaussian noise, and data with 5% multiplication Gaussian noise.

**Data-driven joint inversion.** For the joint inversion, we again use four different data sets; Figure 8 for an example of the datum  $H$  generated from the illuminating source (19) in this case. The optimization algorithm and the termination tolerances are set to be the same in the previous numerical experiment. Table 1 and Table 2 list respectively  $L^2$  errors in the reconstruction of  $\gamma$  and  $\sigma$  with different pair of hyper-parameters  $(J, \alpha_0)$  in Algorithm 1 and noise-free recorded internal data. In general, we note that smaller  $\alpha_0$  and larger  $J$  lead to better reconstructions, but it is not monotone. When  $J \geq 3$  or  $\alpha_0 \leq 10^{-8}$ , the accuracy of the inversion stage does not become better as  $J$  becomes larger or  $\alpha_0$  becomes smaller. To get better resolution, one needs to adjust the hyper-parameters in optimization algorithm. For simplicity, we will use  $(J, \alpha_0) = (3, 0)$  for the rest of simulations in this numerical experiment.

$J \backslash \alpha_0$	0	1e-05	1e-06	1e-07	1e-08	1e-09
1	1.0374e-02	1.3882e-01	7.1773e-02	4.1070e-02	8.0771e-03	8.6503e-03
2	7.5163e-03	9.6056e-02	6.7081e-02	2.1226e-02	6.1786e-03	6.6277e-03
3	5.9652e-03	9.4665e-02	6.4279e-02	1.5911e-02	6.6814e-03	6.2090e-03
4	7.2499e-03	9.2371e-02	4.1357e-02	1.0659e-02	8.6483e-03	7.6470e-03

Table 1:  $L^2$  errors in the reconstruction of  $\gamma$  with different pair of hyper-parameters  $(J, \alpha_0)$  in Algorithm 1 for Numerical Experiment (II) with noise-free data.

To test the stability of the proposed coupled scheme, we add Gaussian noise with zero mean and 5% standard derivation to the data used. Figure 9 presents the surface plots of the initial data for step one (10) and step two (11). Figure 10 displays the reconstructed diffusion field, as well as the reconstructed absorption fields. The layouts of Figure 10 and Figure 9 are the same with Figure 6 and Figure 5, respectively. We observe that the reconstructions are fairly accurate in general. Though the resolution of the reconstructions from the noisy

$J \backslash \alpha_0$	0	1e-05	1e-06	1e-07	1e-08	1e-09
1	7.0129e-05	1.5375e-03	6.5928e-04	3.1494e-04	8.6445e-05	9.5192e-05
2	5.8688e-05	6.4392e-04	5.0289e-04	1.6665e-04	8.4444e-05	6.2425e-05
3	5.4014e-05	6.3150e-04	5.0589e-04	1.0760e-04	5.4986e-05	5.2783e-05
4	7.2869e-05	6.4397e-04	3.6059e-04	9.0858e-05	6.3943e-05	4.4396e-05

Table 2: Same as Table 1 but for the reconstruction of  $\sigma$ .

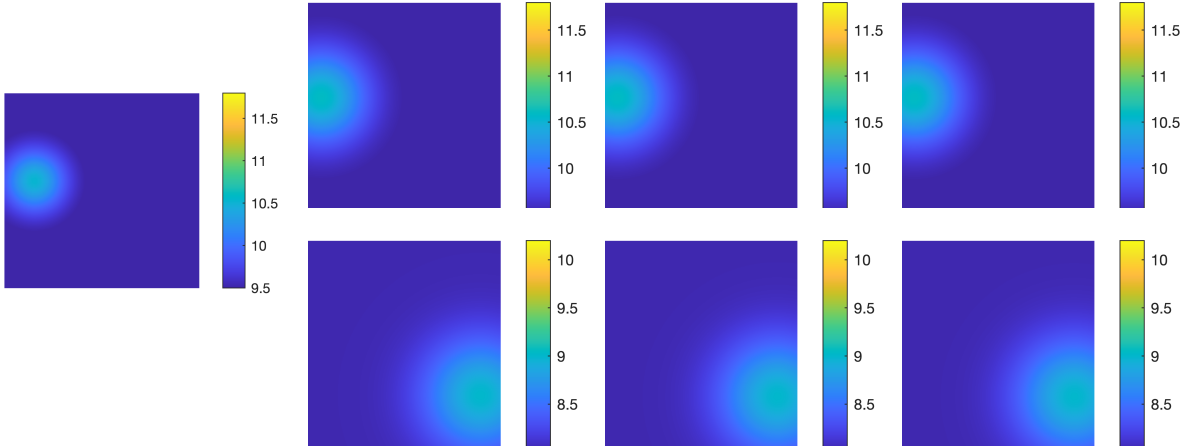


Figure 9: Reconstructions at each stage of the inversion process in Numerical Experiment (II). From left to right are: the initial reconstruction of  $\gamma$  as the solution to (10) (first column), the first step of reconstruction of  $(10^3\gamma, 50\sigma)$  by (11) with noise-free data (second column), with data containing 5% additive Gaussian noise (third column), and with data containing 5% of multiplicative Gaussian noise.

data is not as good as the one from the noise-free data, the bump locations for both the diffusion and the absorption fields are clear and accurate.

## 4.2 The acoustic inverse problem

For the wave propagation model problem (15)-(16), we again select the computational domain to be  $\Omega = (0, 1) \times (0, 1)$ . The illuminating sources are placed on the top boundary of the domain, and a periodic boundary condition is imposed on the left and the right boundaries. A homogeneous Neumann boundary condition is enforced at the bottom boundary.

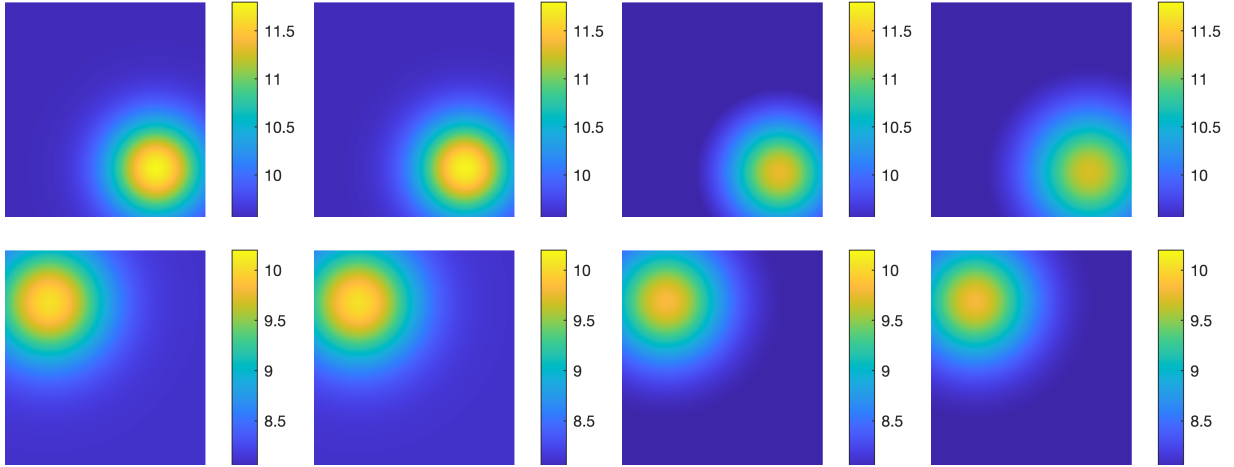


Figure 10: Joint inversion of  $(10^3\gamma, 50\sigma)$  in Numerical Experiment (II). Shown from left to right are: true coefficients, reconstruction from noise-free data, reconstruction from data with 5% additive Gaussian noise, and reconstruction from data with 5% multiplication Gaussian noise.

The wave propagation model (15) then has the following form:

$$\begin{aligned}
\frac{1}{\kappa(\mathbf{x})} \frac{\partial^2 u(t, \mathbf{x})}{\partial t^2} - \Delta \left( \frac{1}{\rho(\mathbf{x})} u(t, \mathbf{x}) \right) &= 0, & (t, \mathbf{x}) \in (0, T] \times (0, 1)^2, \\
\frac{1}{\rho(\mathbf{x})} \frac{\partial u}{\partial z}(t, x, 1) &= S(t, x), & (t, x) \in (0, T] \times (0, 1), \\
\frac{1}{\rho(\mathbf{x})} \frac{\partial u}{\partial z}(t, x, 0) &= 0, & (t, x) \in (0, T] \times (0, 1), \\
u(t, 0, y) &= u(t, 1, y), & (t, y) \in (0, T) \times (-1, 0), \\
u(0, \mathbf{x}) = \frac{\partial u}{\partial t}(0, \mathbf{x}) &= 0, & \mathbf{x} \in (0, 1) \times (0, 1).
\end{aligned} \tag{25}$$

This is the setup in ultrasound transmission tomography [25]; see the setup in Figure 11.

We use the time-domain stagger-grid finite difference scheme that adopts a second-order in both the time and the spatial directions to solve the wave equation (25), then record the wave signal starting at time  $t_0 = 0$  until the termination time  $T$  for each time step. The spatial grid is taken to be the uniform Cartesian grid  $(x_i, y_j) = (i\Delta x, -1 + j\Delta y)$ ,  $i, j = 0, 1, \dots, M$  with  $\Delta x = \Delta y = 1/M$ . The receivers are equally placed on the bottom boundary, coinciding with the grid points, namely, there are  $M + 1$  receivers for each pair of  $(\kappa, \rho)$ . We then record the measured data of the form (16) for the reconstructions.

**Numerical Experiment (III).** It is clear that learning stage of our data-driven two-stage joint inversion procedure is independent of the physical model involved, besides of the fact that we use the physical model to constrain the learning process so that the learned relation is consistent with the underlying physical model. Therefore, here we omit the learning stage

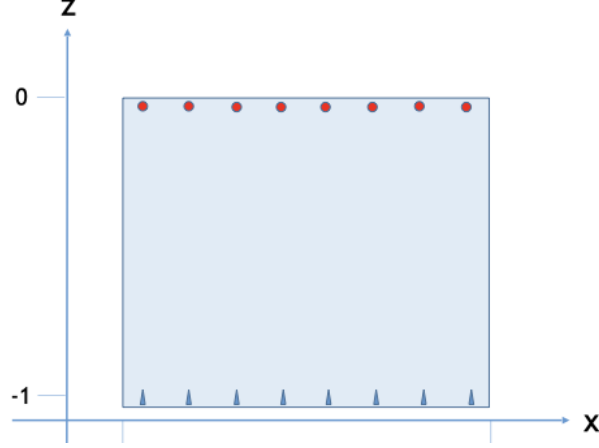


Figure 11: The computational setup for the inverse wave propagation problem (25). Detectors (blue triangles) are placed on bottom boundary of the domain, while sources (red dots) are placed on the top boundary.

to save space but focus on the joint reconstruction. The true density  $\rho$  in our numerical experiment takes the form

$$\rho(x, y) = 1 + 0.2e^{-\frac{(x-0.2)^2+(y+0.2)^2}{2 \times 0.03^2}} + 0.3e^{-\frac{(x-0.6)^2+(y+0.6)^2}{2 \times 0.04^2}}, \quad (26)$$

and the corresponding modulus bulk  $\kappa(x, z)$  takes the form

$$\kappa(x, y) = \begin{cases} 1.1 \sum_{i=0}^3 c_i \rho^i(x - 0.04, y + 0.58), & (x, y) \in [0.1, 0.4] \times [-0.94, -0.64], \\ \sum_{i=0}^3 c_i \rho^i(x - 0.18, y - 0.4), & (x, y) \in [0.58, 1] \times [-0.42, 0], \\ \sum_{i=0}^3 c_i \rho^i(x, y), & \text{otherwise,} \end{cases}$$

where  $c_0 = 1, c_1 = 0.15, c_2 = 0.2, c_3 = 0.05$ .

To mimic the effect of inaccuracy of the learning process, we add some randomness to the coefficient  $\kappa$ . More precisely, for any  $(x, y) \in (0, 1) \times (0, 1)$ ,  $\kappa(x, y)$  is perturbed with probability 0.5, independently of the others, by an amount normally distributed with mean 0 and standard deviation 0.1, namely,

$$\tilde{\kappa}(x, y) = \begin{cases} \kappa(x, y) + \text{normrnd}(0, 0.1), & \text{with a probability 0.5,} \\ \kappa(x, y), & \text{with a probability 0.5.} \end{cases} \quad (27)$$

For the purpose of illustration, we show in Figure 12 the time series wave signals at the bottom surface generated from the top source  $S(t, \mathbf{x})$ ,

$$S(t, \mathbf{x}) = e^{-\frac{(x-0.8)^2}{0.12}} - e^{-\frac{(x-0.2)^2}{0.12}}, \quad \mathbf{x} = (x, y) \quad (28)$$

from the density field  $\rho$  in (26) and the bulk modulus  $\kappa$  in (27). Shown from top to bottom are the wave signals without noise, with 10% additive Gaussian noise, and with 10% multiplication Gaussian noise, respectively. For this particular example, we employ a uniform time step size  $\Delta t = 0.005$ , and the time window size  $T = 5$ .

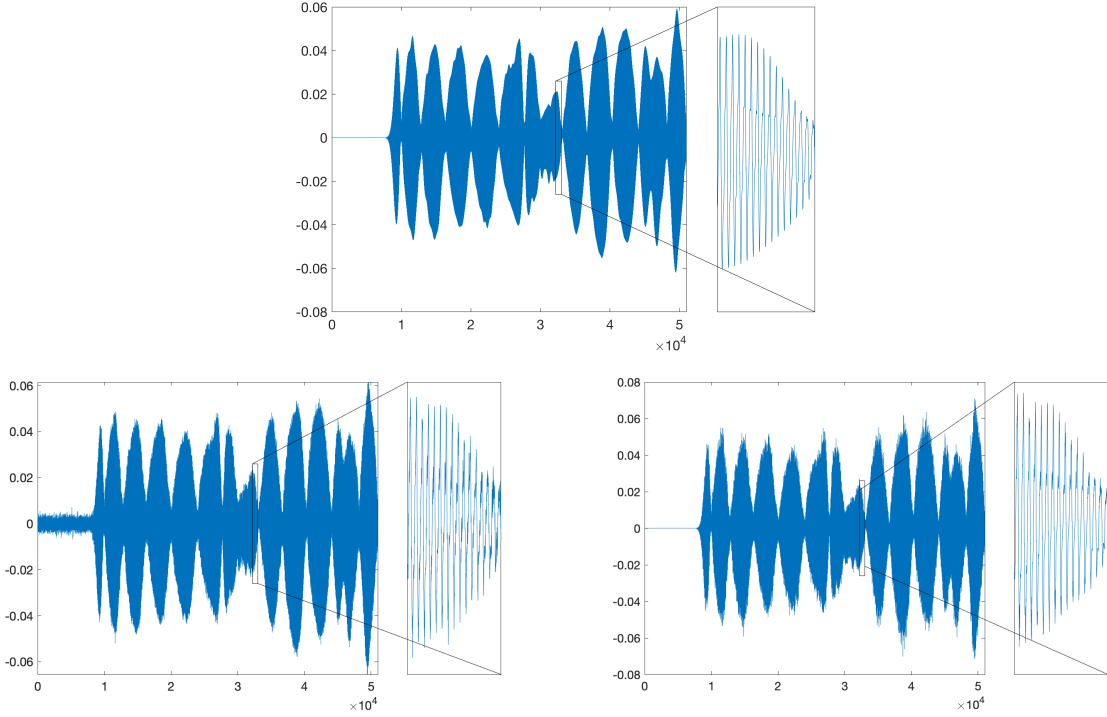


Figure 12: Recorded wave signals at the bottom surface generated from the wave equation (25) with the top external source (28), the density  $\rho$  (26) and bulk modulus  $\kappa$  (27). The top panel display the noise-free recorded signals; the bottom panel, from the left to the right shows the recorded signal with 10% additive Gaussian noise, and with 10% multiplication Gaussian noise, respectively.

The optimization algorithm for the joint reconstruction is set with the termination tolerances  $10^{-8}$  for both the first-order optimality condition and the updating step size. In addition, the hyper-parameters in Algorithm 1 is set to be  $(\alpha, J) = (0, 3)$ .

We present in Figure 13 the surface plots of the initial data for the initial reconstruction by (10) and the initial reconstruction of (11). The first column shows the initial data for searching the density field  $\rho$  when solving (10) while from the second to the fourth column we plot the initial data for searching  $(\rho, \kappa)$  when solving (11). As before, such data are obtained by solving (10) and then applying the relation (27).

The final reconstruction results for  $(\rho, \kappa)$ , with noise-free and noise data, are shown in Figure 14. The  $L^2$  errors in the reconstructions are summarized in Table 3. For this particular set of simulations, the reconstructions of both the density and the bulk modulus are fairly accurate, even with noisy data.

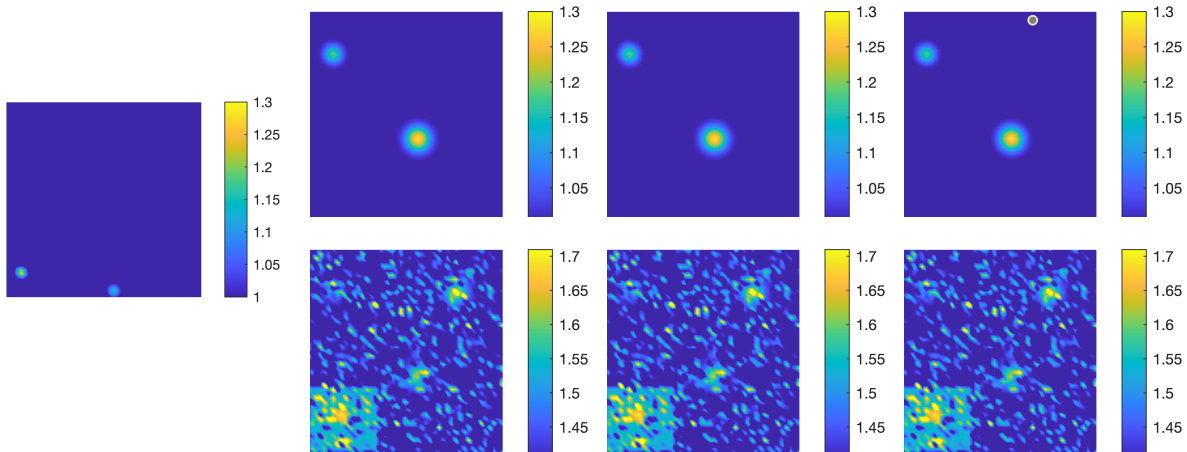


Figure 13: Reconstructions of  $(\kappa, \rho)$  at each stage of the joint inversion process for Numerical Experiment (III). From left to right are respectively:  $\rho$  as the solution of (10), the first step of reconstruction of  $(\kappa, \rho)$  by (11) from noise free data, from data with 10% additive Gaussian noise, and from data with 10% multiplication Gaussian noise.

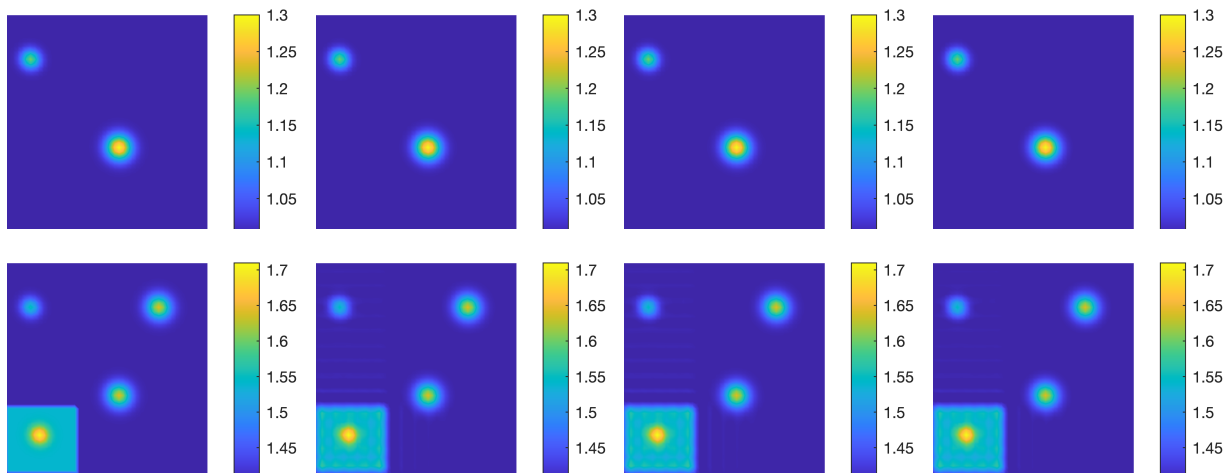


Figure 14: Reconstruction results of  $(\rho, \kappa)$  for Numerical Experiment (III). Show from left to right are: the true coefficients, the reconstruction with noise-free data, the reconstruction with data containing 10% additive Gaussian noise, and the reconstruction with data containing 10% multiplication Gaussian noise.

## 5 Impact of learning inaccuracy on reconstruction

While numerical examples in rather academic environment show great success in learning relations between the coefficients from given data, it is not possible to learn the exact relation between the unknowns in practice, even if such an exact relation exists. In other words, the map  $\mathcal{N}_{\hat{\theta}}$  that we learned is only an approximation to the true relation. In this section, we show that, under reasonable assumptions on the inverse problems, when the learning error

data \ fields	noise-free	10% additive noise	10% multiplicative noise
	<i>step one</i>		
$\rho$	7.7252e-03	7.7281e-03	1.0724e-02
$\kappa$	1.0198e-01	1.0198e-01	1.0190e-01
	<i>step two</i>		
$\rho$	4.6633e-04	2.6205e-04	1.0499e-03
$\kappa$	7.6104e-03	7.5901e-03	7.7240e-03

Table 3:  $L^2$  errors in the reconstructions from different data in Numerical Experiments (III). Shown are results from step one (i.e. solution to (10)) (top row) and step two (i.e. solution to (11)) (bottom row) respectively.

is under control, the error it caused in the joint reconstruction is also under control.

We will use the following standard notations in the rest of the paper. We denote by  $L^p(\Omega)$  ( $1 \leq p \leq \infty$ ) the usual space of Lebesgue integrable functions on  $\Omega$ , and  $W^{k,p}(\Omega)$  the Sobolev space of functions whose  $j$ th derivatives ( $0 \leq j \leq k$ ) are in  $L^p(\Omega)$ . We use the short notation  $\mathcal{H}^k(\Omega) := W^{k,2}(\Omega)$ . The set of functions whose derivatives up to  $k$  are continuous in  $\Omega$  is denoted by  $\mathcal{C}^k(\Omega)$ . We denote by  $\mathcal{B}(\Omega)$  the set of strictly positive functions bounded between two constants  $\underline{\alpha}$  and  $\bar{\alpha}$ ,

$$\mathcal{B}(\Omega) = \{f(\mathbf{x}) : \Omega \mapsto \mathbb{R} : 0 < \underline{\alpha} \leq f(\mathbf{x}) \leq \bar{\alpha} < \infty, \forall \mathbf{x} \in \Omega\}.$$

For the simplicity of presentation, we assume that the domain  $\Omega$  is bounded with smooth boundary  $\partial\Omega$ .

## 5.1 Joint inversion of the diffusion model

For the joint inversion problem with the diffusion model we introduced in Section 3.1, we make the following assumptions:

- (A-i) the boundary value of the diffusion coefficient  $\gamma$ ,  $\gamma|_{\partial\Omega} > 0$ , is known *a priori*;
- (A-ii) we have sufficient number of data set  $H$  such that the absorption coefficient  $\sigma$  is uniquely determined when the relation  $\gamma = \mathcal{N}_\theta(\sigma)$  is known;
- (A-iii) the boundary condition  $S(\mathbf{x}) > 0$  is the restriction of a smooth function on  $\partial\Omega$ , and is such that the solution  $u$  to the diffusion equation (13) satisfies  $u \geq \varepsilon$  for some  $\varepsilon > 0$ .

The assumptions are here only to simplify the presentation as none of the assumptions is essential. In fact, (A-i) can be removed with additional boundary data as shown in [39], (A-ii) is true when data corresponding to two well-chosen boundary conditions are available [5], and (A-iii) is true when  $\gamma$  and  $\sigma$  are non-negative and smooth enough [41].

Following the calculations of [40], we can show the result below.

**Theorem 5.1.** *Let  $\sigma \in \mathcal{C}^1(\Omega) \cap \mathcal{B}$  and  $\tilde{\sigma} \in \mathcal{C}^1(\Omega) \cap \mathcal{B}$  be the absorption coefficients reconstructed from (13)- (14) with the relations  $\gamma = \mathcal{N}_\theta(\sigma)$  and  $\tilde{\gamma} = \mathcal{N}_{\tilde{\theta}}(\tilde{\sigma})$  respectively. Assuming that the operators  $\mathcal{N}_\theta$  and  $\mathcal{N}_{\tilde{\theta}} : \mathcal{C}^1(\Omega) \cap \mathcal{B} \mapsto \mathcal{C}^1(\Omega) \cap \mathcal{B}$  are sufficiently smooth. Then, under the assumptions (A-i)-(A-iii), there exists a constant  $\mathfrak{c}$  such that*

$$\left\| \frac{\tilde{\sigma} - \sigma}{\tilde{\sigma}} \right\|_{\mathcal{H}^1(\Omega)} \leq \mathfrak{c} \left( \|\mathcal{N}_{\tilde{\theta}}(\tilde{\sigma}) - \mathcal{N}_{\tilde{\theta}}(\sigma)\|_{\mathcal{H}^1(\Omega)} + \|\mathcal{N}_{\tilde{\theta}}(\sigma) - \mathcal{N}_\theta(\sigma)\|_{\mathcal{H}^1(\Omega)} \right) \left\| \frac{H}{\sigma} \right\|_{W^{1,\infty}(\Omega)}. \quad (29)$$

*Proof.* Let  $u$  and  $\tilde{u}$  be the solution to (13) corresponding to  $(\gamma := \mathcal{N}_\theta(\sigma), \sigma)$  and  $(\tilde{\gamma} := \mathcal{N}_{\tilde{\theta}}(\tilde{\sigma}), \tilde{\sigma})$  respectively. Then we have

$$\begin{aligned} -\nabla \cdot \mathcal{N}_\theta(\sigma) \nabla u(\mathbf{x}) + \sigma(\mathbf{x})u(\mathbf{x}) &= 0, & \text{in } \Omega \\ \mathbf{n} \cdot \mathcal{N}_\theta(\sigma) \nabla u + \ell u(\mathbf{x}) &= S(\mathbf{x}), & \text{on } \partial\Omega. \end{aligned}$$

and

$$\begin{aligned} -\nabla \cdot \mathcal{N}_{\tilde{\theta}}(\tilde{\sigma}) \nabla \tilde{u}(\mathbf{x}) + \tilde{\sigma}(\mathbf{x})\tilde{u}(\mathbf{x}) &= 0, & \text{in } \Omega \\ \mathbf{n} \cdot \mathcal{N}_{\tilde{\theta}}(\tilde{\sigma}) \nabla \tilde{u} + \ell \tilde{u}(\mathbf{x}) &= S(\mathbf{x}), & \text{on } \partial\Omega. \end{aligned}$$

With the assumptions (A-i)-(A-iii) as well as the assumption on the positivity of the coefficient pairs  $(\mathcal{N}_\theta(\sigma), \sigma)$  and  $(\mathcal{N}_{\tilde{\theta}}(\tilde{\sigma}), \tilde{\sigma})$ , the above diffusion equations admit unique solutions  $u \in \mathcal{C}^2(\bar{\Omega})$  and  $\tilde{u} \in \mathcal{C}^2(\bar{\Omega})$  by classical elliptic theory [16, 20]. Moreover,  $M \geq u, \tilde{u} \geq \varepsilon$  for some  $\varepsilon > 0$  and  $M > 0$ .

Let  $w := u - \tilde{u}$ . It is straightforward to verify that  $w$  solves

$$\begin{aligned} -\nabla \cdot \mathcal{N}_{\tilde{\theta}}(\tilde{\sigma}) \nabla w + \tilde{\sigma}(\mathbf{x})w &= -\nabla \cdot (\mathcal{N}_{\tilde{\theta}}(\tilde{\sigma}) - \mathcal{N}_\theta(\sigma)) \nabla u + (\tilde{\sigma} - \sigma)u, & \text{in } \Omega \\ \mathbf{n} \cdot \mathcal{N}_{\tilde{\theta}}(\tilde{\sigma}) \nabla w + \ell w(\mathbf{x}) &= 0, & \text{on } \partial\Omega \end{aligned} \quad (30)$$

where we used the assumption in (A-i), that is, the boundary value of the diffusion coefficient is known, so  $\mathcal{N}_\theta(\sigma)|_{\partial\Omega} = \mathcal{N}_{\tilde{\theta}}(\tilde{\sigma})|_{\partial\Omega}$ . Meanwhile, since  $\sigma$  and  $\tilde{\sigma}$  are reconstructed from the same data  $H$ , we have that

$$0 = \sigma u - \tilde{\sigma} \tilde{u} = \tilde{\sigma} w - (\tilde{\sigma} - \sigma)u. \quad (31)$$

This gives us, from (30), that  $w$  solves the equation

$$\begin{aligned} -\nabla \cdot \mathcal{N}_{\tilde{\theta}}(\tilde{\sigma}) \nabla w(\mathbf{x}) &= -\nabla \cdot (\mathcal{N}_{\tilde{\theta}}(\tilde{\sigma}) - \mathcal{N}_\theta(\sigma)) \nabla u, & \text{in } \Omega \\ \mathbf{n} \cdot \mathcal{N}_{\tilde{\theta}}(\tilde{\sigma}) \nabla w + \ell w(\mathbf{x}) &= 0, & \text{on } \partial\Omega. \end{aligned}$$

With the assumptions given, this equation for  $w$  is uniformly elliptic. By standard elliptic estimate [16, 20], it follows that

$$\|w\|_{\mathcal{H}^1(\Omega)} \leq \|\nabla \cdot (\mathcal{N}_{\tilde{\theta}}(\tilde{\sigma}) - \mathcal{N}_\theta(\sigma)) \nabla u\|_{L^2(\Omega)} \leq \|u\|_{W^{1,\infty}(\bar{\Omega})} \|\mathcal{N}_{\tilde{\theta}}(\tilde{\sigma}) - \mathcal{N}_\theta(\sigma)\|_{\mathcal{H}^1(\Omega)}.$$

Using the fact that

$$\mathcal{N}_{\tilde{\theta}}(\tilde{\sigma}) - \mathcal{N}_\theta(\sigma) = \mathcal{N}_{\tilde{\theta}}(\tilde{\sigma}) - \mathcal{N}_{\tilde{\theta}}(\sigma) + \mathcal{N}_{\tilde{\theta}}(\sigma) - \mathcal{N}_\theta(\sigma),$$

we can further write the above bound into

$$\|w\|_{\mathcal{H}^1(\Omega)} \leq \|u\|_{W^{1,\infty}(\bar{\Omega})} \left( \|\mathcal{N}_{\tilde{\theta}}(\tilde{\sigma}) - \mathcal{N}_{\tilde{\theta}}(\sigma)\|_{\mathcal{H}^1(\Omega)} + \|\mathcal{N}_{\tilde{\theta}}(\sigma) - \mathcal{N}_{\theta}(\sigma)\|_{\mathcal{H}^1(\Omega)} \right).$$

On the other hand, we have from (31) that

$$\left\| \frac{(\tilde{\sigma} - \sigma)}{\tilde{\sigma}} u \right\|_{\mathcal{H}^1(\Omega)} \leq \|w\|_{\mathcal{H}^1(\Omega)}.$$

Therefore, we arrive at

$$\left\| \frac{(\tilde{\sigma} - \sigma)}{\tilde{\sigma}} u \right\|_{\mathcal{H}^1(\Omega)} \leq \|u\|_{W^{1,\infty}(\bar{\Omega})} \left( \|\mathcal{N}_{\tilde{\theta}}(\tilde{\sigma}) - \mathcal{N}_{\tilde{\theta}}(\sigma)\|_{\mathcal{H}^1(\Omega)} + \|\mathcal{N}_{\tilde{\theta}}(\sigma) - \mathcal{N}_{\theta}(\sigma)\|_{\mathcal{H}^1(\Omega)} \right).$$

The proof is complete after using the fact that  $u$  is bounded from below and  $u = \frac{H}{\sigma}$ .  $\square$

This result says that when the operators  $\mathcal{N}_{\theta}$  and  $\mathcal{N}_{\tilde{\theta}}$  are sufficiently close to each other, in which case  $\|\mathcal{N}_{\theta}(\sigma) - \mathcal{N}_{\tilde{\theta}}(\sigma)\|_{\mathcal{H}^1(\Omega)}$  is small, and  $\mathcal{N}_{\tilde{\theta}}$  is sufficiently smooth, in which case  $\|\mathcal{N}_{\tilde{\theta}}(\tilde{\sigma}) - \mathcal{N}_{\tilde{\theta}}(\sigma)\|_{\mathcal{H}^1(\Omega)}/\|\tilde{\sigma} - \sigma\|_{\mathcal{H}^1(\Omega)}$  is small, the reconstructions based on those relations are also sufficiently close to each other. In other words, the impact of learning error on the joint reconstruction is under control.

## 5.2 Joint inversion of the wave model

We now investigate the same issue for the acoustic wave model (15)- (16) in Section 3.2. To simplify the notation, we perform change of variables  $\kappa \rightarrow 1/\kappa$  and  $\rho \rightarrow 1/\rho$ , and consider relations between the new variables:  $\rho = \mathcal{N}_{\theta}(\kappa)$ . We make the following assumptions:

(B-i) the boundary value of the density  $\rho$ ,  $\rho|_{\partial\Omega} > 0$ , is known *a priori*;

(B-ii)  $S(t, \mathbf{x}) > 0$  is the restriction of a  $\mathcal{C}^{\infty}$  function on  $\partial\Omega$ .

(B-iii) the problem of determining  $\kappa$  (with fixed  $\rho$ ) from data  $\Lambda_{\kappa} : S \mapsto H$  can be stably solved in the sense that  $\|\tilde{\kappa} - \kappa\|_{W^{1,\infty}} \leq C \|\Lambda_{\tilde{\kappa}} - \Lambda_{\kappa}\|_{\mathcal{H}^{1/2}((0,T) \times \partial\Omega) \mapsto \mathcal{H}^{3/2}((0,T) \times \partial\Omega)}$  for some  $C > 0$ .

The problem in (B-ii), that is, determining  $\kappa$  from data  $\Lambda_{\kappa}$ , has been extensively studied. Uniqueness of the reconstruction problem has been proved by the method of boundary control; see for instance [7, 26] and references therein. Global stability such as what we assumed here is not known. Our main objective is to see the impact of uncertainty in  $\rho$  on the reconstruction of  $\kappa$ , not how accurate we can reconstruct  $\kappa$ . This assumption is necessary but also reasonable.

**Theorem 5.2.** *Under the assumptions (B-i)-(B-iii), let  $\kappa \in W^{1,\infty}(\Omega) \cap \mathcal{B}$  and  $\tilde{\kappa} \in W^{1,\infty}(\Omega) \cap \mathcal{B}$  be reconstructed from (15)- (16) with the relations  $\rho = \mathcal{N}_{\theta}(\kappa)$  and  $\tilde{\rho} = \mathcal{N}_{\tilde{\theta}}(\tilde{\kappa})$  respectively. Assuming that the operators  $\mathcal{N}_{\theta}$  and  $\mathcal{N}_{\tilde{\theta}} : W^{1,\infty}(\Omega) \cap \mathcal{B} \mapsto W^{1,\infty}(\Omega) \cap \mathcal{B}$  are sufficiently smooth. Then there exists a constant  $\mathbf{c}$  such that*

$$\|\tilde{\kappa} - \kappa\|_{W^{1,\infty}(\Omega)} \leq \mathbf{c} \left( \|\mathcal{N}_{\tilde{\theta}}(\tilde{\kappa}) - \mathcal{N}_{\tilde{\theta}}(\kappa)\|_{W^{1,\infty}(\Omega)} + \|\mathcal{N}_{\tilde{\theta}}(\kappa) - \mathcal{N}_{\theta}(\kappa)\|_{W^{1,\infty}(\Omega)} \right). \quad (32)$$

*Proof.* By the assumptions on the smoothness and boundedness of the coefficients  $\kappa$  and  $\tilde{\kappa}$  as well as the operators  $\mathcal{N}_\theta$  and  $\mathcal{N}_{\tilde{\theta}}$ , the equation (15) with coefficients  $(\kappa, \mathcal{N}_\theta(\kappa))$  and  $(\tilde{\kappa}, \mathcal{N}_{\tilde{\theta}}(\tilde{\kappa}))$  are well-posed [16]. We denote by  $p$  and  $\tilde{p}$  the corresponding solutions. We define  $w := \tilde{p} - p$ . Then  $w$  solves

$$\begin{aligned} \tilde{\kappa} \frac{\partial^2 w}{\partial t^2} - \nabla \cdot (\mathcal{N}_{\tilde{\theta}}(\tilde{\kappa})w) &= -(\tilde{\kappa} - \kappa) \frac{\partial^2 p}{\partial t^2} + \nabla \cdot (\mathcal{N}_{\tilde{\theta}}(\tilde{\kappa}) - \mathcal{N}_\theta(\kappa)) \nabla p, & \text{in } (0, T] \times \Omega \\ \mathbf{n} \cdot \mathcal{N}_{\tilde{\theta}} \nabla w &= 0, & \text{on } (0, T] \times \partial\Omega \\ w(0, \mathbf{x}) = \frac{\partial w}{\partial t}(0, \mathbf{x}) &= 0, & \text{in } \Omega \end{aligned}$$

where we used the assumption in (B-i). Let  $G$  be adjoint Green function of this problem, that is,  $G$  is the solution to

$$\begin{aligned} \tilde{\kappa} \frac{\partial^2 G}{\partial t^2} - \nabla \cdot (\mathcal{N}_{\tilde{\theta}}(\tilde{\kappa})G) &= 0, & \text{in } (0, T] \times \Omega \\ \mathbf{n} \cdot \mathcal{N}_{\tilde{\theta}} \nabla G &= \delta(t-s)\delta(\mathbf{x}-\mathbf{y}), & \text{on } (0, T] \times \partial\Omega \\ G(T, \mathbf{x}; s, \mathbf{y}) = \frac{\partial G}{\partial t}(T, \mathbf{x}; s, \mathbf{y}) &= 0, & \text{in } \Omega. \end{aligned}$$

Then for any  $(t, \mathbf{x}) \in (0, T) \times \partial\Omega$ , we have

$$w(t, \mathbf{x}) = \int_0^T \int_\Omega G(s, \mathbf{y}; t, \mathbf{x}) \left[ (\tilde{\kappa} - \kappa) \frac{\partial^2 p}{\partial t^2} - \nabla \cdot (\mathcal{N}_{\tilde{\theta}}(\tilde{\kappa}) - \mathcal{N}_\theta(\kappa)) \nabla p \right] d\mathbf{y} ds.$$

Using the fact that the reconstructions are from the same data, we have that

$$w(t, \mathbf{x}) = 0, \quad \text{on } (0, T] \times \partial\Omega.$$

Therefore, we have

$$\int_\Omega (\tilde{\kappa} - \kappa) \int_0^T G(s, \mathbf{y}; t, \mathbf{x}) \frac{\partial^2 p}{\partial t^2} ds d\mathbf{x} = \int_\Omega \int_0^T G \nabla \cdot (\mathcal{N}_{\tilde{\theta}}(\tilde{\kappa}) - \mathcal{N}_\theta(\kappa)) \nabla p d\mathbf{y} ds.$$

This can be further written into, using the assumption that  $\mathcal{N}_{\tilde{\theta}}(\tilde{\kappa}) = \mathcal{N}_\theta(\kappa)$  on  $\partial\Omega$ ,

$$\int_\Omega (\tilde{\kappa} - \kappa) \left( \int_0^T G(s, \mathbf{y}; t, \mathbf{x}) \frac{\partial^2 p}{\partial t^2} ds \right) d\mathbf{x} = \int_\Omega \left( \mathcal{N}_{\tilde{\theta}}(\tilde{\kappa}) - \mathcal{N}_\theta(\kappa) \right) \left( \int_0^T \nabla G \cdot \nabla p ds \right) d\mathbf{y}.$$

Under the assumptions we made, by classical theory [26], the integral operator on the left, denote by  $\mathcal{G}$ , with kernel  $\left( \int_0^T G(s, \mathbf{y}; t, \mathbf{x}) \frac{\partial^2 p}{\partial t^2} ds \right)$  is invertible. We therefore write the above equation into the form

$$\tilde{\kappa} - \kappa = \mathcal{G}^{-1} \left[ \int_\Omega \left( \mathcal{N}_{\tilde{\theta}}(\tilde{\kappa}) - \mathcal{N}_\theta(\kappa) \right) \left( \int_0^T \nabla G \cdot \nabla p ds \right) d\mathbf{y} \right] := \mathcal{G}^{-1} \mathcal{G}_\Delta \left( \mathcal{N}_{\tilde{\theta}}(\tilde{\kappa}) - \mathcal{N}_\theta(\kappa) \right).$$

With the assumption in (B-iii), we have a version of  $\mathcal{G}^{-1} : \mathcal{H}^{1/2}((0, T] \times \partial\Omega) \mapsto W^{1,\infty}(\Omega)$  that is bounded. Moreover,  $\mathcal{G}_\Delta : \mathcal{H}_1^\infty(\bar{\Omega}) \mapsto \mathcal{H}^{1/2}((0, T) \times \partial\Omega)$  is a bounded operator. The result of (32) then follows directly.  $\square$

We emphasize again here that the assumption in (B-iii) is necessary to get the result in this theorem. While this assumption is not verified mathematically, it is necessary for the uncertainty characterization here. On the other hand, the assumption is not essential in the sense that we are only interested in the relative change to the solution caused by the difference between the relationships  $\mathcal{N}_\theta$  and  $\mathcal{N}_{\tilde{\theta}}$ . This relative change is small as long as  $\mathcal{N}_{\tilde{\theta}} - \mathcal{N}_\theta$  is small (even if  $\kappa$  might not have been reconstructed perfectly).

## 6 Concluding remarks

In this work, we provided a proof-of-principle study on a computational framework for data-driven joint reconstruction problems, or multiple coefficient inverse problems, for partial differential equations. We developed a method that fusing data with the mathematical model involved to learn relations between different unknowns to be reconstructed. Our method provides a learned model that is consistent with the underlying physical model for reconstruction purpose. Moreover, we use the learned model to guide the joint reconstruction instead of using it as a hard constraint. This gives the flexibility for the joint reconstruction algorithm to find solutions outside of the training dataset.

Our main objective for this study is not to replace classical inversion methods with learning methods but rather using additional historical data to help solve the joint reconstruction problem that can not be stably solved without the necessary relations between the unknowns. Moreover, due to the fact that the data-driven modeling part of the computation can be conducted offline, we are not concerned with the computational cost introduced by the supplementary dataset. The online model-based joint inversion, even though now done with an additional loop, has computational cost comparable to a standard joint inversion algorithm.

Our study is based on the assumption that there is a relation (2) between the  $f$  and  $g$  data that is available to us. This is indeed the case in many physics-based inverse problems where  $f$  and  $g$  are physical coefficients that are related. Our study would not make any sense, and the learning process for the data-driven modeling process will not converge to a stable solution, if this assumption does not hold. When the assumption indeed hold, and the joint inversion problem is stable with respect to the data, our preliminary sensitivity analysis show that the reconstruction is stable, in appropriate sense, with respect to the inaccuracy in the learning result.

There is critical issue that we left without discussion in this work, that is, should we learn the map from  $f$  to  $g$ , that is,  $\mathcal{N}_\theta$  in our presentation, or the map from  $g$  to  $f$  (which would be roughly the inverse of  $\mathcal{N}_\theta$ ). The answer to this depends on how much *a priori* information we have on those maps. It is well-known in deep learning research that a smoothing map, corresponding to information compression process, is in general easier to learn (since the parameterization of the map require smaller number of parameters) than its map. Therefore, we should choose to learn the smoother one, whether it is  $\mathcal{N}_\theta$  or its inverse.

# Acknowledgments

This work is partially supported by the National Science Foundation through grants DMS-1913309, DMS-1937254 and EAR-2000850.

## A Details on computational implementation

We discuss in this appendix some technical details on the computational implementation of the algorithms.

### A.1 Learning with polynomial models

As we have emphasized, our main objective is not to learn the exact relation between the coefficients but only a reasonable approximation between them to improve the joint inversion process. Therefore, we are interested in learning the relation with low-order polynomials that have small number of degree of freedom (which in turn require small amount of training data points).

The polynomial model (9) is constructed in a way that the different components of the output are completely independent to each other. In other words, we did not impose any constraint on the coefficient  $\theta_{1,\alpha}, \dots, \theta_{K,\alpha}$  even though some constraints should be enforced. We do, however, need to force the predicted coefficient  $g$  to be physically relevant. For instance, for the two joint inversion problems we considered, we impose the constraint that  $g$  is positive and is bounded from above and below by some known constants  $\underline{\alpha}$  and  $\bar{\alpha}$ , that is

$$\underline{\alpha} \leq \sum_{k=1}^K \left( \sum_{|\alpha| \leq n} \theta_{k,\alpha} P_{\alpha}(\hat{\mathbf{f}}) \right) \varphi_k(\mathbf{x}) \leq \bar{\alpha}. \quad (33)$$

This is a linear constraint on the components of the polynomial coefficient  $\theta$ .

**Generalization to piecewise smooth case.** While the generalized Fourier parameterization (7) is a global method, we can extend it to the case of piecewise smooth coefficients by constructing the basis on subdomains of  $\Omega$ . The polynomial relation (9) is now dependent on the subdomains, that is,

$$\hat{\mathbf{g}}_{\zeta} := \left( \sum_{|\alpha| \leq n} \theta_{1,\alpha,\zeta} P_{\alpha}(\hat{\mathbf{f}}_{\zeta}), \dots, \sum_{|\alpha| \leq n} \theta_{j,\alpha,\zeta} P_{\alpha}(\hat{\mathbf{f}}_{\zeta}), \dots, \sum_{|\alpha| \leq n} \theta_{K,\alpha,\zeta} P_{\alpha}(\hat{\mathbf{f}}_{\zeta}) \right) \quad (34)$$

where the subscript  $\zeta$  is used to highlight the fact that the corresponding quantity is on the  $\zeta$ -th subdomain. When the polynomial relation is learned directly from the coefficient pair (3), the learning process on the subdomains have the same amount of data and can be done in parallel. In our model-consistent learning framework, however, this poses additional challenges as it increases the number of parameters in the representation of the operator,

unless we impose additional constraints on the relations on different subdomains (for instance by asking them to be sufficiently close to each other).

## A.2 Network representation and training

To illustrate the feasibility of our approach for problems where the relation between the coefficients are more complicated than what we have discussed, we implemented a neural network representation to benchmark the polynomial representation.

In our implementation of the autoencoder architecture, each substructure (that is, the encoder, the decoder, or the predictor) is a standard fully connected network of  $L + 1$  layers. To be precise, let  $n^\ell$  be the width of layer  $\ell$  ( $0 \leq \ell \leq L$ ), and  $\Theta^\ell(\mathbf{x}) : \mathbb{R}^{n^{\ell-1}} \rightarrow \mathbb{R}^{n^\ell}$  the standard linear transform

$$\Theta^\ell(\mathbf{x}) = \mathbf{W}^{\ell-1}\mathbf{x} + \mathbf{b}^{\ell-1},$$

where  $\mathbf{W}^{\ell-1} \in \mathbb{R}^{n^\ell \times n^{\ell-1}}$  and  $\mathbf{b}^{\ell-1} \in \mathbb{R}^{n^\ell}$  are respectively the weight and bias for layer  $\ell$ . Then the network output  $\mathbf{y}$  corresponding to input  $\mathbf{x}$  is described by the following iterative propagation scheme

$$\begin{aligned} P^0 &= \mathbf{x}, \\ P^\ell &= \phi(\Theta^\ell(P^{\ell-1})), \quad \ell = 1, 2, \dots, L, \\ \mathbf{y} &= \Theta^{L+1}(P^L). \end{aligned} \tag{35}$$

where  $\phi$  is the nonlinear activation function and  $\phi(\mathbf{x})$  for any  $d$ -vector is understood as the  $d$ -vector  $(\phi(x_1), \dots, \phi(x_d))$ . We denote by  $\theta$  the set of parameters  $\{\mathbf{W}^\ell, \mathbf{b}^\ell\}_{\ell=1}^{L+1}$  for the network.

The training of the autoencoder network is done by minimizing a loss function  $\mathcal{L}(\theta)$  that combines the loss for the encoder-decoder substructure and another loss term for the encoder-predictor substructure. More precisely, we minimize

$$\begin{aligned} \mathcal{L}(\theta) := & \frac{1}{2N|H|} \sum_{h \in H} \sum_{k=1}^N \|\mathcal{A}_h(f_k, \widetilde{\mathcal{N}}_\theta^{ep}(f_k)) - u_{h,k}\|_Y^2 \\ & + \frac{1}{2N} \sum_{k=1}^N \|\mathcal{F}(g_k) - \mathcal{N}_\theta^{ep}(\mathcal{F}(f_k))\|_{\widetilde{X}}^2 + \frac{1}{2N} \sum_{k=1}^N \|\mathcal{F}(f_k) - \mathcal{N}_\theta^{ed}(\mathcal{F}(f_k))\|_{\widetilde{X}}^2, \end{aligned} \tag{36}$$

where the operators  $\mathcal{N}_\theta^{ep} = P_\theta \circ E_\theta$  and  $\mathcal{N}_\theta^{ed} = D_\theta \circ E_\theta$  are respectively the encoder-predictor and encoder-decoder networks, and  $\widetilde{\mathcal{N}}_\theta^{ep} := \mathcal{F}^{-1} \circ \mathcal{N}_\theta^{ep} \circ \mathcal{F}$  is the relation between the coefficients  $f$  and  $g$  in the physical space  $X$ . The first two terms in the loss functions are for the encoder-predictor substructure and the third term is for the encoder-decoder substructure. The first term in the loss function is to enforce the model-consistency requirement.

## References

- [1] A. ABUBAKAR, G. GAO, T. M. HABASHY, AND J. LIU, *Joint inversion approaches for geophysical electromagnetic and elastic full-waveform data*, *Inverse Problems*, 28 (2012). 055016.

- [2] V. AKÇELİK, G. BIROS, AND O. GHATTAS, *Parallel multiscale Gauss-Newton-Krylov methods for inverse wave propagation*, in Proceedings of the 2002 ACM/IEEE Conference on Supercomputing, 2002, pp. 1–15.
- [3] S. R. ARRIDGE, *Optical tomography in medical imaging*, Inverse Probl., 15 (1999), pp. R41–R93.
- [4] E. BACHMANN AND J. TROMP, *Source encoding for viscoacoustic ultrasound computed tomography*, J. Acoust. Soc. Am., 147 (2020), pp. 3221–3235.
- [5] G. BAL AND K. REN, *Multi-source quantitative PAT in diffusive regime*, Inverse Problems, 27 (2011). 075003.
- [6] G. BAL AND G. UHLMANN, *Inverse diffusion theory of photoacoustics*, Inverse Problems, 26 (2010). 085010.
- [7] M. I. BELISHEV, *Boundary control in reconstruction of manifolds and metrics (the bc method)*, Inverse Problems, 13 (1997), p. R1.
- [8] M. BELLASSOUED, D. JELLALI, AND M. YAMAMOTO, *Lipschitz stability in an inverse problem for a hyperbolic equation with a finite set of boundary data*, Applicable Analysis, 87 (2008), pp. 1105–1119.
- [9] S. BERNARD, V. MONTEILLER, D. KOMATITSCH, AND P. LASAYGUES, *Ultrasonic computed tomography based on full-waveform inversion for bone quantitative imaging*, Phys. Med. Bio., 62 (2017), pp. 7011–7035.
- [10] L. BORCEA, V. DRUSKIN, A. MAMONOV, AND M. ZASLAVSKY, *Untangling the nonlinearity in inverse scattering with data-driven reduced order models*, Inverse Problems, 34 (2018). 065008.
- [11] J. R. CANNON AND P. DUCHATEAU, *An inverse problem for a nonlinear diffusion equation*, SIAM J. Appl. Math., 39 (1980), pp. 272–289.
- [12] B. CRESTEL, G. STADLER, AND O. GHATTAS, *A comparative study of structural similarity and regularization for joint inverse problems governed by PDEs*, Inverse Problems, 35 (2018), p. 024003.
- [13] T. DING, K. REN, AND S. VALLELIAN, *A one-step reconstruction algorithm for quantitative photoacoustic imaging*, Inverse Problems, 31 (2015). 095005.
- [14] B. ENGQUIST, B. D. FROESE, AND Y. YANG, *Optimal transport for seismic full waveform inversion*, Commun. Math. Sci., 14 (2016), pp. 2309–2330.
- [15] I. EPANOMERITAKIS, V. AKÇELİK, O. GHATTAS, AND J. BIELAK, *A Newton-CG method for large-scale three-dimensional elastic full-waveform seismic inversion*, Inverse Problems, 24 (2008). 034015.
- [16] L. C. EVANS, *An Introduction to Stochastic Differential Equations*, American Mathematical Society, Providence, RI, 2013.
- [17] X. FENG, Q. REN, C. LIU, AND X. ZHANG, *Joint acoustic full-waveform inversion of crosshole seismic and ground-penetrating radar data in the frequency domain*, Geophysics, 82 (2017), pp. H41–H56.

- [18] L. A. GALLARDO AND M. A. MEJU, *Characterization of heterogeneous near-surface materials by joint 2D inversion of DC resistivity and seismic data*, Geophys. Res. Lett., 30 (2003). 1658.
- [19] L. A. GALLARDO AND M. A. MEJU, *Joint two-dimensional dc-resistivity and seismic travel time inversion with cross-gradients constraints*, J. Geophys. Res., 109 (2004). B03311.
- [20] D. GILBARG AND N. S. TRUDINGER, *Elliptic Partial Differential Equations of Second Order*, Springer-Verlag, Berlin, 2000.
- [21] D. GILTON, G. ONGIE, AND R. WILLETT, *Neumann networks for linear inverse problems in imaging*, arXiv:1901.03707v2, (2020).
- [22] L. GUASCH, O. CALDERÓN AGUDO, M. X. TANG, P. NACHEV, AND M. WARNER, *Full-waveform inversion imaging of the human brain*, Digit. Med., 3 (2000). 28.
- [23] T. M. HABASHY, W. C. CHEW, AND E. Y. CHOW, *Simultaneous reconstruction of permittivity and conductivity profiles in a radially inhomogeneous slab*, Radio Science, 21 (1986), pp. 635–645.
- [24] E. HABER AND D. OLDENBURG, *Joint inversion: a structural approach*, Inverse Problems, 13 (1997), pp. 63–77.
- [25] M. C. HESSE, L. SALEHI, AND G. SCHMITZ, *Nonlinear simultaneous reconstruction of inhomogeneous compressibility and mass density distributions in unidirectional pulse-echo ultrasound imaging*, Physics in Medicine & Biology, 58 (2013), pp. 6163–6178.
- [26] V. ISAKOV, *Inverse Problems for Partial Differential Equations*, Springer-Verlag, New York, second ed., 2006.
- [27] A. JAVAHERIAN, F. LUCKA, AND B. T. COX, *Refraction-corrected ray-based inversion for three-dimensional ultrasound tomography of the breast*, Inverse Problems, 36 (2020). 125010.
- [28] J. JOST, *Partial Differential Equations*, Springer Science & Business Media, 2012.
- [29] A. KIRSCH AND O. SCHERZER, *Simultaneous reconstructions of absorption density and wave speed with photoacoustic measurements*, SIAM J. Appl. Math., 72 (2013), pp. 1508–1523.
- [30] F. KNOLL, M. HOLLER, T. KOESTERS, R. OTAZO, K. BREDIES, AND D. K. SODICKSON, *Joint MR-PET reconstruction using a multi-channel image regularizer*, IEEE Trans. Med. Imag., 36 (2017), pp. 1–16.
- [31] F. LI, U. VILLA, S. PARK, AND M. A. ANASTASIO, *Three-dimensional stochastic numerical breast phantoms for enabling virtual imaging trials of ultrasound computed tomography*, arXiv:2106.02744, (2021).
- [32] Q. LIU, S. BELLER, W. LEI, D. PETER, AND J. TROMP, *Preconditioned BFGS-based uncertainty quantification in elastic full waveform inversion*, arXiv:2009.12663, (2020).
- [33] B. D. LOWE AND W. RUNDELL, *The determination of multiple coefficients in a second-order differential equation from input sources*, Inverse Problems, 9 (1993), pp. 469–482.
- [34] F. LUCKA, M. PÉREZ-LIVA, B. E. TREEBY, AND B. T. COX, *High resolution 3D ultrasonic breast imaging by time-domain full waveform inversion*, arXiv:2102.00755, (2021).

- [35] T. P. MATTHEWS AND M. A. ANASTASIO, *Joint reconstruction of the initial pressure and speed of sound distributions from combined photoacoustic and ultrasound tomography measurements*, *Inverse Problems*, 33 (2017). 124002.
- [36] T. P. MATTHEWS, J. POUDEL, L. LI, L. V. WANG, AND M. A. ANASTASIO, *Parameterized joint reconstruction of the initial pressure and sound speed distributions for photoacoustic computed tomography*, *SIAM J. Imaging Sci.*, 11 (2018), pp. 1560–1588.
- [37] R. G. PRATT, *Seismic waveform inversion in the frequency domain, Part 1: Theory and verification in a physical scale model*, *Geophysics*, 64 (1999), pp. 888–901.
- [38] K. REN, G. BAL, AND A. H. HIELSCHER, *Frequency domain optical tomography based on the equation of radiative transfer*, *SIAM J. Sci. Comput.*, 28 (2006), pp. 1463–1489.
- [39] K. REN, H. GAO, AND H. ZHAO, *A hybrid reconstruction method for quantitative photoacoustic imaging*, *SIAM J. Imag. Sci.*, 6 (2013), pp. 32–55.
- [40] K. REN AND S. VALLÉLIAN, *Characterizing impacts of model uncertainties in quantitative photoacoustics*, *SIAM/ASA J. Uncertainty Quantification*, 8 (2020), pp. 636–667. arXiv:1812.02876.
- [41] K. REN AND R. ZHANG, *Nonlinear quantitative photoacoustic tomography with two-photon absorption*, *SIAM J. Appl. Math.*, 78 (2018), pp. 479–503.
- [42] A. REZAEI, M. DEFRISE, G. BAL, C. MICHEL, M. CONTI, C. WATSON, AND J. NUYTS, *Simultaneous reconstruction of activity and attenuation in time-of-flight pet*, *IEEE Trans. Med. Imaging*, 31 (2012), pp. 2224–2233.
- [43] L. ROQUES AND M. CRISTOFOL, *The inverse problem of determining several coefficients in a nonlinear Lotka-Volterra system*, *Inverse Problems*, 28 (2012). 075007.
- [44] P. STEFANOV AND G. UHLMANN, *Instability of the linearized problem in multiwave tomography of recovery both the source and the speed*, *Inverse Problems and Imaging*, 7 (2013), pp. 1367–1377.
- [45] W. W. SYMES, *Migration velocity analysis and waveform inversion*, *Geophysical Prospecting*, 56 (2008), pp. 765–790.
- [46] J. TROMP, C. TAPE, AND Q. LIU, *Seismic tomography, adjoint methods, time reversal and banana-doughnut kernels*, *Geophys. J. Int.*, 160 (2005), pp. 195–216.
- [47] J. WISKIN, B. MALIK, D. BORUP, N. PIRSHAFIEY, AND J. KLOCK, *Full wave 3D inverse scattering transmission ultrasound tomography in the presence of high contrast*, *Scientific Reports*, 10 (2020). 20166.